



## 1 Introduction

The deep sea is one of the remotest habitats on Earth and its biological diversity is largely unexplored. 76 % of the inhabitants in the deep pelagic zone emit light to communicate, attract prey or to protect themselves [1]. The trait of bioluminescence is distributed over a diverse range of marine species, from bacteria to fish [2]. Over the last years the distribution and quantification of bioluminescence in the deep sea and individual luminescent organisms have been studied using a variety of observational techniques [1,3–6]. Most in-situ observation techniques rely on actively triggering the light production by disturbing the environment and stimulating the organisms, since spontaneous emission does not occur at statistically sufficient rates for observation times in the order of hours [7–9]. In this context, spontaneous emission refers to light emission which is not intentionally stimulated by observers, similar as in [8]. The free-fall lander observations in the Atlantic Ocean off Cape Verde has detected 5 events per hour when fixing the sensor 250 m above the sea floor at 4700 m leading to no active stimulation due to movements of the sensor [7]. With these studies, similarities between emitted bioluminescence flashes have been observed. Most organisms emit a single light flash or a series of flashes; a rapid increase of the luminosity indicates the start of a flash which - after reaching its peak value - is decaying exponentially with a time constant significantly longer than that of the initial rise. Studies have characterized such flash lightcurves from various species by the duration, the maximum photon flux and the total photon emission of the flash [2,9–30]. An overview of these characteristics is provided in table 1. Most species in the benthic and pelagic zone emit light flashes with their emission maxima within the range of  $\lambda = 450 - 520$  nm [2] which corresponds to the wavelength window of maximum light transmission in seawater [31].

**Table 1**  
Characteristics of bioluminescent flashes taken from [2, 9, 10].

Characteristics	Values
Mean duration of flash (s)	0.1 – 59.0
Maximum photon flux (photons $s^{-1}$ )	$4.9 \cdot 10^7 - 6.4 \cdot 10^{12}$
Total light emission (photons $flash^{-1}$ )	$2.4 \cdot 10^8 - 2.3 \cdot 10^{13}$
Spectral wavelength (nm)	450 – 520

For years, deep sea neutrino telescopes have been monitoring and recording the light activity. These telescopes aim to detect Cherenkov radiation caused by charged secondary particles, which are induced by high-energy cosmic neutrino interactions with constituents of water molecules. The records of these telescopes were used to analyze the dynamics of deep sea bioluminescence [4, 32–34]. The majority of the

recorded bioluminescence is assumed to be triggered by sea currents and turbulence around the detectors [4, 33]. Therefore, the challenge to observe spontaneous bioluminescence remains. In addition to analysis of long-term temporal changes, the experimental setup and long-term observations of deep sea neutrino telescopes offers also the possibility to analyze light emission of individual organisms and relatively rare events of spontaneous bioluminescence.

In this paper, we present a method to reconstruct the movement and characteristic lightcurves of individual biological sources in the deep sea with data of a neutrino telescope. In particular, we use both synthetic, as well as measured data of the ANTARES neutrino telescope located 40 km off the French coast on the bottom of the Mediterranean Sea ( $42^\circ 48'N$ ,  $6^\circ 10'E$ ) and anchored to the sea floor at a depth of 2475 m. The method enabled us to do the localization of a luminescent organism using ANTARES data and the simultaneous reconstruction of the corresponding emitted bioluminescence lightcurve.

To do so, we developed a generative model of the measurement process of a neutrino detector and the signal generation of the biological sources to understand the origin of the measured data. The model parameters such as source movement and characteristic lightcurves are reconstructed by a Variational Bayesian Inference algorithm, called Metric Gaussian Variational Inference (MGVI) [35]. The NIFTy (Numerical Information Field Theory) framework [36, 37] provides an implementation of the MGVI algorithm and has been used to obtain results of this work.

The paper is structured as follows; in section 2 we summarize the data provided by the ANTARES experiment and used for the reconstruction. In section 3, the proposed method is explained by describing the generative model in detail and highlighting our assumptions. In section 4, simulations and reconstructions on synthetic data sets are performed to discuss the opportunities and limitations of the model. The first localizations of deep sea organisms and reconstructions of their emitted bioluminescence lightcurves using the ANTARES detector are presented and discussed in section 5.

## 2 Data

The ANTARES telescope consists of twelve lines that are distributed over an area of  $0.1 \text{ km}^2$ . The lines have a length of 480 m and are placed at a distance of around 60 m to each other. Each line, excluding the twelfth, contains 25 storeys with a vertical separation of 14.5 m between them. The 5 top storeys of line 12 are not equipped with photomultipliers, but with different acoustic instruments [38]. The first storey of

each line is located around 100 m above the seabed. A storey is defined as a collection of three optical modules each containing a photomultiplier tube (PMT). The optical modules (OMs) are oriented downward looking under 45 degrees (zenith angle of 135 degrees) and with an angle of 120 degrees to each other in horizontal directions [39, 40]. A schematic view of the ANTARES setup is given in figure 1.

Each optical module measures the light activity in terms of photon hits. The photon hits recorded in time frames of  $\Delta t = 104.858$  ms are directly sent to shore and the rates of each time frame are calculated [41]. According to a trigger system the photon hits are stored for a specific period of time depending on the type of trigger. In the following, only data samples with detection periods covering fully the bioluminescence lightcurve of interest are used to analyze the biological behavior. About 1 to 2 of such recordings are saved per day containing around 2 minutes of continuous raw data.

In addition to the photon count rates, the position and orientation, as well as the efficiency of each optical module is monitored precisely [40, 42]. The origin of the internal coordinate system used for the positioning of the OMs is located in the center of the detector volume. This internal coordinate system of ANTARES indicates the west-east direction as x-axis and the south-north direction as y-axis. The vertical direction is given by the z-axis [40, 43]. Within this work we introduce the naming convention of each optical module as a tuple of line number and number of optical module ( $l, n_{om}$ ). The optical modules of one line are consecutively numbered starting at the bottom of the line.

An example data file is shown in figure 2. In order to represent the setup of the ANTARES detector, the photon counts of one storey are grouped together. In the figure, an almost constant background for each optical module with photon count rates around 40 – 60 kHz can be identified. This background is assumed to be induced by  $^{40}\text{K}$  nuclear decays, bioluminescence, photomultiplier intrinsic noise and radioactive decays in the sea water and in the glass sphere [44]. Furthermore, we assume to recognize two bioluminescence flashes that are recorded by six optical modules over two storeys. The occurrence times of the flashes are 40 s and 84 s after a trigger started the recording. The flash recorded at  $t = 40$  s surpassed the threshold limit of optical module (4, 43), i.e. the readout electronics is saturated which let the recorded photon rate drop to zero for this detector for a short period. These two flashes are analyzed in section 5.

The attenuation length of light in the sea water at the ANTARES site was measured by the ANTARES

Collaboration. The light attenuation of water depends on its chemical and physical properties. Therefore, various measurements of the water light transmission properties have been made from 1997 to 2010 using an isotropic light source that emits blue light [31, 45]. The light attenuation includes the effect of water absorption of light as well as the impact of scattered photons reaching the detector [31]. A summary of the results of the study is given in table 2. Variation in light attenuation depends on the amount of particles in the water that depends on oceanographic processes, see [34]. These additional measurements of the state of the detector and the environment are crucial to perform reasonable reconstructions of biological light sources.

**Table 2**  
Light attenuation length in sea water at ANTARES site including only statistical errors [31, 45].

Measurement	$l_{\text{att}}$
July 1998	$60.6 \pm 0.4$ m
March 1999	$51.9 \pm 0.7$ m
June 2000	$46.4 \pm 1.9$ m
May 2008 to March 2010	$\sim 50 - 60$ m

### 3 Methods

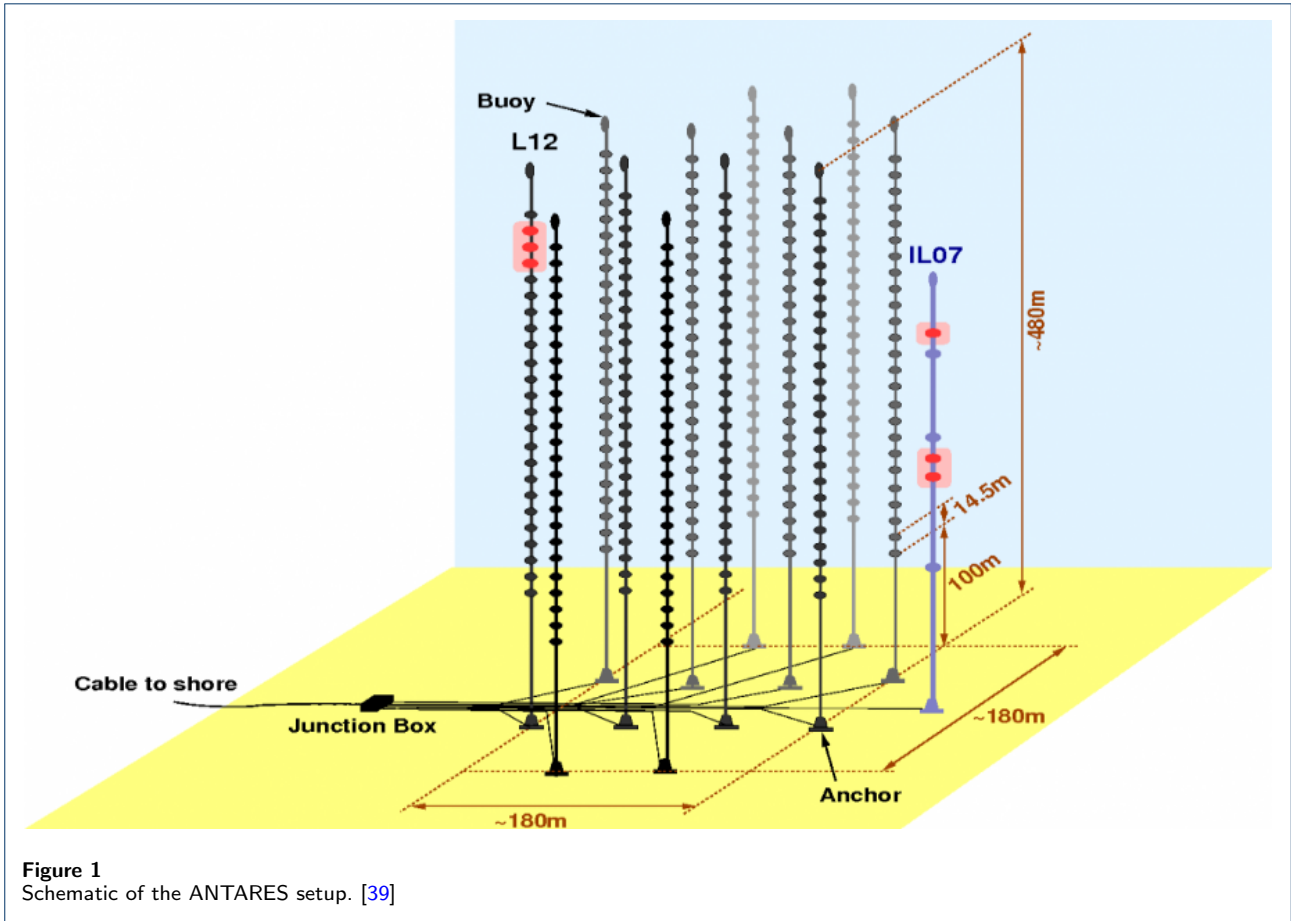
The data provided by the ANTARES experiment and knowledge about the organisms and their environment in the deep sea allow us to derive a mathematical model of the data generation process. This model depends on a set of model parameters  $\xi$  and is able to describe a luminescent organism emitting a flash lightcurve, the propagation of the signal in the deep sea, and the detection of photon hits at a neutrino detector.

According to Bayes' theorem, measuring photon hits  $d$  updates the prior knowledge on  $\xi$ , expressed as probability density function  $\mathcal{P}(\xi)$ . The resulting posterior density  $\mathcal{P}(\xi|d)$  can be calculated as follows by knowing the likelihood  $\mathcal{P}(d|\xi)$  of the obtained data, given  $\xi$ , and the marginal probability of the data  $\mathcal{P}(d)$ ,

$$\mathcal{P}(\xi|d) = \frac{\mathcal{P}(d|\xi) \mathcal{P}(\xi)}{\mathcal{P}(d)}. \quad (1)$$

In case of high dimensionality and complexity of a model the posterior distribution  $\mathcal{P}(\xi|d)$  is often intractable. To overcome this issue we approximate this distribution with a simpler distribution  $\tilde{\mathcal{P}}_{\eta}(\xi)$  depending on variational parameter  $\eta$ . Within this work the posterior approximation is performed by the MGVI algorithm [35, 46].

In order to apply Bayes' update rule and perform the posterior approximation a detailed understanding of the likelihood is crucial. First, we discuss the measurement process of a photon detector and derive an



expression for the likelihood of multiple optical modules. Second, we build a mathematical model for the light emission of an organism and the light propagation through water reaching the photon detector. We explain each aspect of our model in detail, beginning with the generic formula of the expected photon number arriving at one optical module.

### 3.1 Likelihood and measurement process

The optical modules of neutrino telescopes detect single photons. Individual photon hits can be treated as independent events and therefore the photon detection is a classical Poisson process. Due to the assumption of Poisson statistics, the photon rate  $r_{i,t}$  over the detection window  $(t - \Delta t, t)$  needs to be converted to the total number of photon hits  $d_{i,t} = \Delta t \cdot r_{i,t}$  detected by optical module  $i$ .

The likelihood of measuring  $d_{i,t}$  photon hits at the optical module  $i$  at time  $t$  for a given expected number of photon hits  $\lambda_{i,t}$  can be written as

$$\mathcal{P}(d_{i,t}|\lambda_{i,t}) = \lambda_{i,t}^{d_{i,t}} \frac{e^{-\lambda_{i,t}}}{d_{i,t}!}. \quad (2)$$

The expected number of photon hits  $\lambda_{i,t}$  is defined as the photon counts over the fixed detection time  $\Delta t$  with. The measurement process is independent at different times  $t, t + \Delta t, \dots$  and at different optical modules  $i, i + 1, \dots$ . Hence, the likelihood of the count data vector  $d$  over a time frame  $\Delta T = N \cdot \Delta t$  with  $N$  discrete time steps and elements  $d_{i,t}$  is the direct product of the single measurement likelihoods,

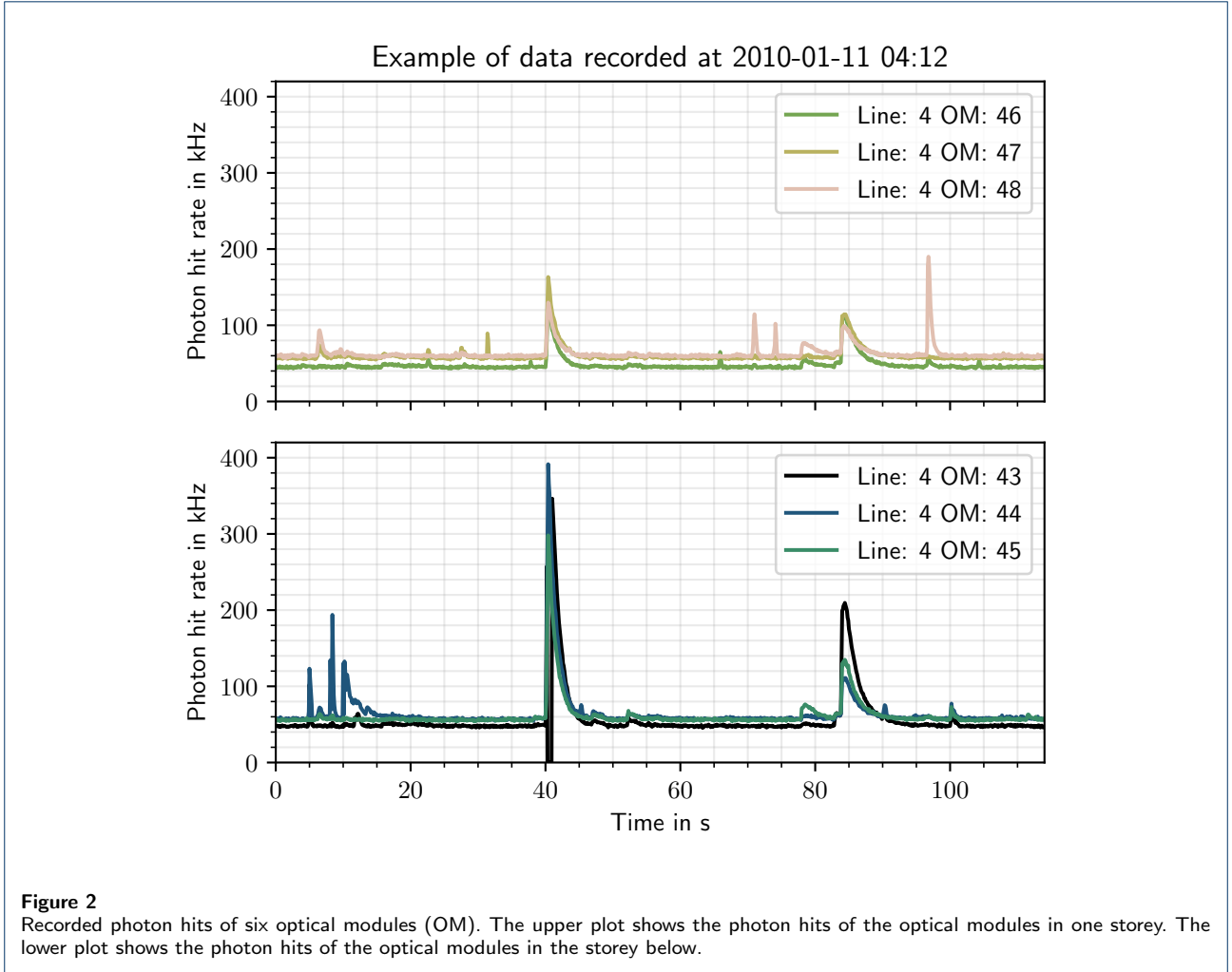
$$\mathcal{P}(d|\lambda) = \prod_i \prod_{t=0}^{N-1} \lambda_{i,t}^{d_{i,t}} \frac{e^{-\lambda_{i,t}}}{d_{i,t}!} = \prod_i \mathcal{P}(d_i, \lambda_i). \quad (3)$$

### 3.2 Signal generation

#### 3.2.1 Expected photon number

The number of expected photons depends highly on the light source itself, but also on specific attributes of the detector and its surroundings. The luminescent organisms are modeled as moving point sources with a position  $\vec{x}(t)$  that generate specific time-varying light patterns spreading isotropically.<sup>[1]</sup> The total amount of

<sup>[1]</sup>The assumption of isotropy is an approximation, but for many of the transparent organisms a reasonable one.



photons emitted by a point source over the detection period  $(t - \Delta t, t)$  is described by the function  $\mathcal{N}(t)$ . Typically  $\mathcal{N}$  is a vector containing the photon numbers of a time frame  $\Delta T$  at  $N$  discrete times with time steps of  $\Delta t$ . The luminosity  $\mathcal{L}$  can be calculated as the rate of emitted photons per second,  $\mathcal{L} = \frac{\mathcal{N}}{\Delta t}$ . Therefore, the number of emitted photons  $\mathcal{N}$  is given by multiplying the luminosity with the time step  $\Delta t$ .

Due to various factors such as detector quality, detector geometry and water absorption, the amount of photons reaching the optical modules is reduced. The efficiency  $\epsilon_i$  of the optical module  $i$  is sampled ( $\leftarrow$ ) from a Gaussian model

$$\epsilon \leftarrow \mathcal{G}(\epsilon - \epsilon_{\text{ANTARES}}, \sigma_\epsilon^2), \quad (4)$$

with efficiencies  $\epsilon_{\text{ANTARES}}$  provided by measurements of the ANTARES Collaboration and inferable standard deviation  $\sigma_\epsilon$ . Deviations need to be allowed because missing optical modules lead to wrong assumptions about the efficiencies in one storey (see [42]).

In addition, the photon sensitive area of the optical modules is modeled as a circular surface with an area of  $A_{\text{om}} = \pi r_{\text{om}}^2$ . Only a fraction

$$\frac{A_{\text{om}}}{A_{\text{light}}(r_i(t))} \quad (5)$$

of the emitted photons can hit the detector  $i$  since the photons spread uniformly on the surface of the sphere  $A_{\text{light}}(\vec{r}) = 4\pi \cdot r_i^2(t)$  at a distance  $r_i(t) = |\vec{r}_i(t)|$  from the source. The vector between the light source position  $\vec{x}$  and the detector position  $\vec{p}_i$  is calculated by

$$\vec{r}_i(t) = \vec{p}_i - \vec{x}(t).$$

Furthermore, the angular acceptance and accordingly the orientation of the detector plays an important role. The angular acceptance  $\alpha(\theta_{\text{optical}})$  as a function of the optical angle  $\theta_{\text{optical}}$  is provided by the ANTARES experiment. The cosine of the optical angle depends

on the orientation  $\vec{o}_i$  of the optical module and can be obtained by

$$\cos \theta_{\text{optical}} = \frac{-1}{|\vec{r}_i(t)| |\vec{o}_i|} \vec{r}_i(t) \cdot \vec{o}_i.$$

The polynomial fit of the angular acceptance stated as

$$\alpha(\theta_{\text{optical}}) = \alpha(\vec{r}_i(t), \vec{o}_i) \quad (6)$$

is used to calculate the percentage of photons coming from direction  $\vec{r}_i(t)$  that actually hit the optical module oriented in  $\vec{o}_i$  direction.

Finally, the impact of electromagnetic absorption by water and the photon scattering can be determined by the attenuation length  $l_{\text{att}}$  and the Beer-Lambert law. The fraction of photons reaching the detector after absorption and scattering can be calculated by

$$\frac{\tilde{\mathcal{N}}_i(t)}{\mathcal{N}(t)} = e^{-r_i(t)/l_{\text{att}}} \quad (7)$$

with  $\mathcal{N}(t)$  as defined before being the number of emitted photons and  $\tilde{\mathcal{N}}_i(t)$  the number of photons reaching the distance of the detector  $i$ . Despite small local changes of the water properties in the deep sea the attenuation length  $l_{\text{att}}$  is assumed to be independent of the position of the optical modules. Due to the measurements of the attenuation length mentioned in section 2 (Table 2), which vary over the years, we assume a flat prior distribution for  $l_{\text{att}}$  within the interval  $l_{\text{att}} = (45 \text{ m}, 60 \text{ m})$ . This assumption prevents the reconstruction to adapt unphysical values and thereby stabilizes the inference.

Combining these effects on the emitted photons, the response function for the photon counts  $\lambda_{i,t}$  detected by the optical module  $i$  can be expressed as

$$\lambda_i(t) = \epsilon_i \cdot \mathcal{N}(t) \cdot \alpha(\vec{o}_i, \vec{r}_i(t)) \cdot e^{-\frac{r_i(t)}{l_{\text{att}}}} \frac{A_{\text{om}}}{4\pi \cdot r_i^2(t)}. \quad (8)$$

It is important to highlight that  $\mathcal{N}$  describes the number of photons isotropically emitted by a hypothetical luminescent organism modeled as point source. The complex structure of real biological organisms that may lead to anisotropic emission is not covered by our model. This mismatch between the assumed isotropic model and the real light emission of organisms in the deep sea can lead to unrepresentative uncertainty estimates of the MGVI algorithm, as discussed in section 2. A compact summary of the response function with its high-level parameters is given in table 3. A visualization of the described generative model is given in figure 3 at the end of the section.

### 3.2.2 Luminosity

The bioluminescence lightcurves are assumed to be the dominant feature of the photon counts over time. The luminosity model  $\mathcal{L}(t) = \frac{\mathcal{N}(t)}{\Delta t}$  has to be able to capture all features of a bioluminescence flash and hence be able to provide sensible prior samples.

Since the number of emitted photons is always positive,  $\mathcal{N}(t)$  can be described to sufficient accuracy by a log-normal model. The lightcurve structure does not depend on absolute times  $t$ , but on the relative timing  $\Delta t = t_l - t_k$ . Therefore, a correlated signal  $s(t)$  with a given correlation matrix  $C_{t_l t_k} = C(t_l - t_k)$  is used to model the burst kinetics under the assumption of statistical homogeneity. Combining all prior assumptions the equation for the luminosity model yields

$$\mathcal{N}(t) = e^{s(t)}, \quad (9)$$

with  $s(t)$  sampled from a Gaussian with inferable mean  $\mu_s$  and fixed covariance  $C$ ,

$$s(t) \leftrightarrow \mathcal{G}(s - \mu_s, C). \quad (10)$$

Although we do not know the underlying correlation structure exactly, we can use the recorded lightcurve structure to estimate the correlation. The main motivation for a fixed covariance is to reduce the computation time. Alternatively, the correlation could be inferred as well, as it is done for the source movement in section 3.2.3. The formulation and discussion of a reasonable correlation function as well as the distribution transformations used for the luminosity model can be found in the appendix. The parameters of the luminosity model were chosen such that the attributes of recorded bursts given in table 1 were fulfilled and similar bursts as in figure 2 could be constructed. A compact summary of the function modeling the photon rate with its parameters is given in table 4 and illustrated in figure 3.

### 3.2.3 Source movement

The  $x$ ,  $y$  and  $z$  directions of the movement of the source within the coordinate system of the detector are handled independently from each other. For each direction  $j \in x, y, z$  a velocity vector  $v_j(t)$  can be reconstructed to describe the movement starting at point  $\vec{x}_0 = (x_0, y_0, z_0)$ .

Similarly to the luminosity model, statistical stationarity is assumed for the velocity as a function of time. But instead of using a fixed correlation matrix, this is inferred as well. In contrast to the luminosity model, we do not have access to previous recordings of the

**Table 3**

Overview of the response function with its parameters and their explanations.

$$\lambda_i(t) = \epsilon_i \cdot \mathcal{N}(t) \cdot \alpha(\vec{o}_i, \vec{r}_i(t)) \cdot e^{-\frac{r_i(t)}{l_{\text{att}}}} \frac{A_{\text{om}}}{4\pi \cdot r_i^2(t)}$$

High-level parameters	Explanation
$\epsilon_i$	Detector efficiency of optical module $i$ , assumed constant over time
$\mathcal{N}(t)$	Emitted photons of an isotropic point source emitter, time dependent
$\vec{x}(t)$	Position of biological object, time dependent
$\vec{p}_i$	Position of optical module $i$ , assumed constant over time
$\vec{r}_i(t) = \vec{p}_i - \vec{x}(t)$	Vector from source to optical module $i$
$r_i(t) =  \vec{r}_i(t) $	Distance from source to optical module $i$
$\vec{o}_i$	Orientation of optical module $i$
$\alpha(\vec{o}_i, \vec{r}_i(t))$	Angular acceptance
$l_{\text{att}}$	Attenuation length of light in sea water, assumed constant over time
$A_{\text{om}} = \pi r_{\text{om}}^2$	Effective area of the optical module assuming a circle
$A_{\text{light}} = 4\pi \cdot r_i^2(t)$	Area covered by spherical radiation at the location of optical module $i$

**Table 4**

Overview of the emitted photon number function with its parameters, their explanations and origin.

$$\mathcal{N}(t) = e^{s(t)}$$

Parameters	Explanation	Origin
$s$	Correlated field	$s \leftrightarrow \mathcal{G}(s - \mu_s, C)$
$\mu_s$	Inferable mean	See <a href="#">appendix</a>
$C$	Correlation matrix	Fixed prior value

movement to estimate the correlation. Consequently, the velocity vectors

$$v_j(t) \leftrightarrow \mathcal{G}(v_j - \mu_{v_j}, K) \quad (11)$$

are sampled from a Gaussian with an inferable correlation matrix  $K_{t_l t_k}$  as covariance. The covariance can be set such that sampled velocities meet criteria of biological plausible movements. A detailed discussion about reconstructing correlation functions of a signal can be found in the NIFTy documentation [36] and the corresponding papers [37, 47].

The starting position of the movement  $\vec{x}_0$  is assumed to be drawn from a uniform prior distribution within a box  $j_0 = (j_0^-, j_0^+)$  for each direction  $j \in x, y, z$ ,

$$j_0 \leftrightarrow \mathcal{U}(j_0^-, j_0^+). \quad (12)$$

A reasonable limitation of the source location is possible due to the setup of the ANTARES telescope and the assumption of isotropic light emissions. By detecting the optical module with the highest photon numbers during a bioluminescence flash, source locations outside of a given volume around this module can be excluded.

The absolute position  $\vec{x}(t)$  at time  $t$  can be obtained by integrating the velocity from start time  $t_0$  up to  $t$  and adding the start position  $\vec{x}_0$ . Hence, the expression of the position vector  $\vec{x}(t)$  can be derived as

$$\vec{x}(t) = \vec{x}_0 + \Delta t \cdot \sum_{t_k=t_0}^t \vec{v}(t_k). \quad (13)$$

Distribution transformations between Gaussian distributions and uniform distributions  $x_0(\xi_{x_0})$  are used and discussed in the [appendix](#). A compact summary of the position and movement model with its parameters is given in figure 3 and in table 5.

**Table 5**

Overview of the position and movement model with its parameters, their explanations and origin.

Parameters	Explanation	Origin
$\vec{x}_0$	Starting position $x, y, z$ independent	$j_0 \leftrightarrow \mathcal{U}(j_0^-, j_0^+)$
$(j_0^-, j_0^+)$	Range for uniform distribution	Fixed prior values
$\vec{v}$	Velocity vector $v_x, v_y, v_z$ independent	$v_j \leftrightarrow \mathcal{G}(v_j - \mu_{v_j}, K)$
$\mu_{v_j}$	Inferable mean	See [47]
$K$	Inferable correlation matrix	A priori assumptions

### 3.2.4 Optical background

In addition to the lightcurves emitted by an individual luminescent organism, photons from other sources are detected as well. As mentioned in section 2 an

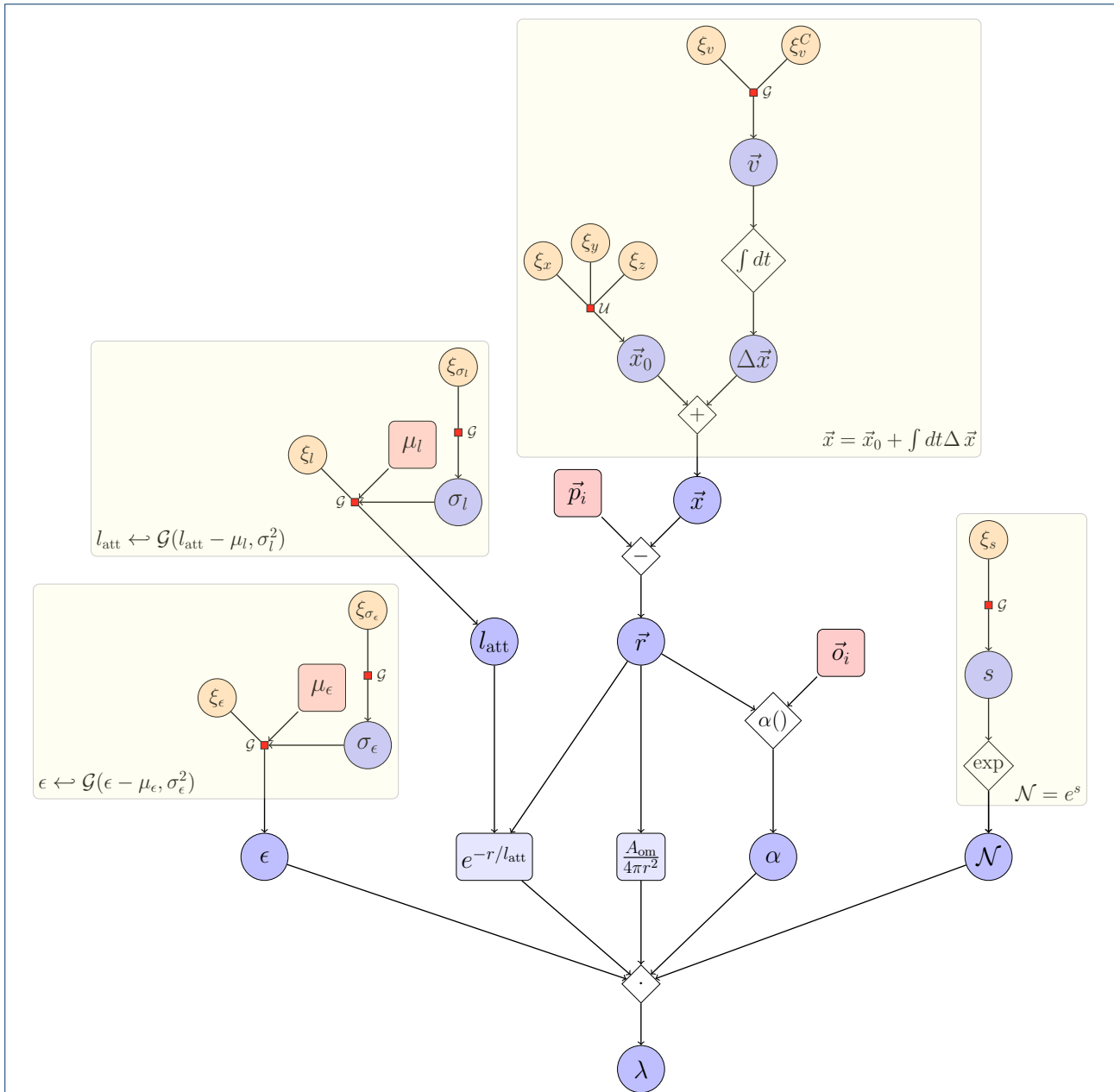


**Figure 3**  
 Generative model of the response function. Blue shapes indicate in quantities that are in principle observable. The standardized variables are colored orange and operations have a diamond shape. The transformations from a standard Gaussian distribution into a target distribution are labeled as a small red square with the target distribution next to it. All red colored values include a priori assumptions, i.e. distribution transformation, detector position and orientation.



almost constant background light is assumed to be induced by nuclear decays and bacterial bioluminescence. We model this optical background as constant offset  $n_{\text{storey}}$  for each individual optical module. Furthermore, we assume that all optical modules of one storey monitor a water volume containing a similar amount of nuclear decays and of small luminescent organisms. Hence, the same constant light background is recorded at one storey. Allowing local variations of the water attributes, each background value  $n_{\text{storey}}$  for one storey is sampled from a Gaussian distribution

$$n_{\text{storey}} \leftarrow \mathcal{G}(n_{\text{storey}} - \mu_n, \sigma_n^2). \quad (14)$$

This leads to the extended response function of an optical module in a given storey

$$\lambda_{i,\text{ext}} = \lambda_i + \epsilon_i \cdot n_{\text{storey}}. \quad (15)$$

### 3.2.5 Reconstruction routine

For the inference of such a complex model we propose a reconstruction routine that is split up into two parts. We first assume a simpler model by neglecting the movement of the source. This assumption reduces the complexity of the model and allows a more stable inference. After analyzing the results of this static reconstruction, one can conclude whether a more complex model including the movement of the source is required. If the data can be reconstructed by the assumption of a static source, the real source does not move or its movement can not be resolved. Observing deviations between the data and its reconstruction imply the need for a better model. In that case the reconstructed position and luminosity are used as initial samples for the dynamic reconstruction. The samples of remaining variables of the model are randomly initiated according to their model priors. This scheme reduces the risk of overfitting to which such a complex model is prone to. In the next section the splitting of the reconstruction is performed on simulated data to analyze this routine, as well as the limitations and opportunities of the model.

## 4 Simulations

In the last section we developed the response function of the expected photon counts of an optical module. Due to the form of the response, being a product of the factors  $\mathcal{N}$ ,  $\epsilon$ ,  $e^{r/l_{\text{att}}}$  and  $\frac{A_{\text{om}}}{4\pi r^2} \cdot \alpha(\vec{r}, \vec{\sigma})$ , increases of one factor can be compensated by decrements of another factor, and vice versa. This leads to a degeneracy between the emitted photon number  $\mathcal{N}$ , the source position  $\vec{x}$ , the efficiency  $\epsilon$  of an optical module and the attenuation length  $l_{\text{att}}$ . This degeneracy can only be

reduced by using the data of multiple OMs and assuming a constant background light. In the following sections we analyze the degeneracy between those variables by performing the reconstruction on synthetic data sets of multiple OMs. First, we focus on a static reconstruction of a simulated static source in order to examine whether the degeneracy can be reduced to such a degree that a light source can be localized and the corresponding bioluminescence lightcurve reconstructed. Secondly, we apply the complete dynamic reconstruction to the simulated static source, as well as a simulated dynamic source. These results are used to discuss the spatial resolution of the reconstruction and the possibility of a movement reconstruction.

For the simulation of static and dynamic sources, the configuration of the ANTARES telescope from some past moment in time is used to create the detector setup. The efficiencies are randomly drawn from Gaussian distributions (equation 4) with fixed standard deviation for each optical module. To simulate a realistic environment, the attenuation length is set to  $l_{\text{att}} = 55$  m and the constant light background of each storey is drawn from a Gaussian distribution (equation 14) with fixed mean  $\mu_n = 50$  kHz and fixed standard deviation  $\sigma_n = 5$  kHz. Further, the shape of a burst is extracted from real data and scaled to reach realistic luminosity values.

The initial position in both cases is manually set to ( $x_0 = 50$  m,  $y_0 = 1$  m,  $z_0 = 23$  m). While the static source stays at its initial position, we simulate a linear movement with a velocity  $v = 0.2 \frac{\text{m}}{\text{s}}$  for the dynamic source. The light signal is detected by 15 optical modules distributed over 5 storeys of one line. The mean of the recorded photon hits of each optical module is calculated according to equation 15. Tables 8 and 11 provide the ground truth observables of the static and dynamic simulated source, respectively.

### 4.1 Static reconstruction of a synthetic static source

The parameters for the initial position of the static inference model (equation 12) used to reconstruct data generated from the static source are provided in table 6. The parameters of the photon number model are given in the appendix. Assumptions about the efficiencies of the optical modules, the attenuation length and the light background are given in table 7. The position and orientation of each optical module used for the simulation are also used for the inference.

Several reconstruction runs were performed, each with a different random seed to assess numerical stability. In order to analyze the degeneracy between source position, luminosity and attenuation length, we compare the reconstructed values with their ground truth summarized in table 8. The position of the light source

**Table 6**

Model parameters of a static inference source. The model is used to reconstruct the photon count data generated from a simulated static source.

Observable	Model	Model parameters
$x$ position	Uniform	$x = (15 \text{ m}, 75 \text{ m})$
$y$ position	Uniform	$y = (-20 \text{ m}, 40 \text{ m})$
$z$ position	Uniform	$z = (15 \text{ m}, 35 \text{ m})$
Flash shape	Correlated signal	See <a href="#">appendix</a>

**Table 7**

Model parameters used to reconstruct the attributes of a simulated telescope and its surroundings.

Observable	Model	Model parameter
$\epsilon$	$\mathcal{G}(\epsilon - \mu_\epsilon, \sigma_\epsilon^2)$ with $\mathcal{G}(\sigma_\epsilon - \mu_{\sigma_\epsilon}, \sigma_{\sigma_\epsilon}^2)$	$\mu_\epsilon = \epsilon_{\text{ANTARES}}$ $\mu_{\sigma_\epsilon} = 0.01,$ $\sigma_{\sigma_\epsilon} = 0.001$
$l_{\text{att}}$	$\mathcal{U}(l_{\text{min}}, l_{\text{max}})$	$l_{\text{min}} = 45 \text{ m},$ $l_{\text{max}} = 60 \text{ m}$
$n_{\text{storey}}$	$\mathcal{G}(n_{\text{storey}} - \mu_n, \sigma_n^2)$	$\mu_n = 50 \text{ kHz},$ $\sigma_n = 5 \text{ kHz}$

$\vec{x} = (50 \text{ m}, 1 \text{ m}, 23 \text{ m})$  could be reconstructed for each run. The ground truth position lies within the given error ranges, which does not include systematic errors. In contrast, for each reconstruction run a different attenuation length was inferred and the reconstructed peak luminosity deviates up to 5% from the ground truth.

We conclude that the degeneracy between the luminosity and the attenuation length, i.e. the fact that any decrease in observed photon counts could either be explained by a shorter attenuation length or a less bright source, still remains for the given data and used model. In future work, a better informed model might help to break the degeneracy. However, this degeneracy has negligible impact on the localization of the source. The ratio of photons counts between the optical modules  $\frac{\lambda_i}{\lambda_j}$ , which is independent of the luminosity and attenuation length, provides information about the source position and hence makes it unambiguously inferrable.

#### 4.2 Dynamic reconstruction of a synthetic static source

As explained in section 3.2.5 the flash lightcurve and the position of the static reconstruction of the previous section are used as the initially assumed position for the dynamic reconstruction. In table 10 the parameters of the dynamic model are summarized. The model parameters of the detector and its environment are the same as in the static reconstruction and provided in table 7.

Since the reconstructions of the remaining observables were already discussed in the previous section and similar results could be observed for assuming a dynamic model, we focus on the discussion about the

velocity. For all runs, a source movement was reconstructed with a mean velocity  $v \simeq 0.01 \frac{\text{m}}{\text{s}}$ . The results of the different reconstruction runs with varying seeds are summarized in table 9.

These results show that a source movement with a mean velocity  $v = 0.01 \frac{\text{m}}{\text{s}}$  can not be distinguished from a static source for this detector setup. This automatically defines a lower bound for the spatial resolution of this method using the ANTARES detector. The spatial resolution depends on the setup of the detector, i.e. number of optical modules and angular acceptance. Therefore, future neutrino telescopes with different detector setups might increase the resolution. In the next section we demonstrate that a movement reconstruction is theoretically possible with the ANTARES setup by applying the method to synthetic data drawn from a simulated dynamic source.

#### 4.3 Complete reconstructions of a dynamic source

##### 4.3.1 Static reconstruction

For the first part of the reconstruction routine, the same model parameters of the detector and source are used as in the static scenario given in table 6 and 7. The results of the reconstruction of a dynamic source using the static model are provided in table 11.

Analyzing the results shows that a dynamic reconstruction might increase the accuracy of the estimates as the static model did not provide an optimal fit. In figure 4 the residuals  $e = \frac{d-\lambda}{\sigma}$  relative to the shot noise of the Poissonian measurement process  $\sigma = \sqrt{\lambda}$  of optical module (4, 44) are presented. During the light flash an increased level of deviations ( $2 < |e| < 5$ ) can be recognized. Residuals of optical module (4, 44) close to zero can be found at  $t_{\text{min}} \simeq 6.3 \text{ s}$ . Detailed analysis shows that the relative residuals are positive  $e > 0$  before the minimum  $t < t_{\text{min}}$  and negative  $e < 0$  afterwards  $t > t_{\text{min}}$ . Even though these variations are only slightly above the shot noise of the measurement process  $\sigma$ , they can be explained by a moving source. Hence, another reconstruction is performed to reduce these residuals by introducing a model for the source movement.

##### 4.3.2 Dynamic reconstruction

We use the same dynamic model as in the previous section 4.3.1. The parameters used to define the source model are given in table 10 and the parameters for the detector setup and its environment are presented in table 7.

The increased level of variations between simulated and reconstructed response of the static model can be almost reduced to  $0 < |e| < 2$  by the dynamic reconstruction as shown in figure 4, a clear improvement over the static model. The reconstructed movement visualized in figure 5 highlights the limits of the

**Table 8**

Ground truth and reconstructed parameters for a static inference source. The synthetic photon count data were generated from the simulated static source. The reconstructed attenuation length is also included.

Observable	Ground truth	Run 1	Run 2	Run 3
$x$ source position (m)	50.00	$49.96 \pm 0.04$	$49.94 \pm 0.04$	$49.96 \pm 0.06$
$y$ source position (m)	1.00	$0.96 \pm 0.07$	$1.03 \pm 0.05$	$0.95 \pm 0.08$
$z$ source position (m)	23.00	$23.03 \pm 0.03$	$22.97 \pm 0.03$	$23.03 \pm 0.03$
Flash duration (s)	5.14	5.14	5.14	5.14
$\mathcal{L}_{\max}$ ( $10^{10}$ Hz)	3.71	$3.66 \pm 0.07$	$3.51 \pm 0.02$	$3.65 \pm 0.01$
Total emission ( $10^{10}$ photons flash $^{-1}$ )	5.20	5.14	4.94	5.13
Attenuation length (m)	55.00	$53.90 \pm 2.09$	$59.94 \pm 0.20$	$54.23 \pm 3.06$

**Table 9**

Ground truth and reconstructed parameters using a dynamic source model. The synthetic photon count data were generated from a simulated static source. The positions are given at the beginning of the observation period  $t_0$ , during the time of highest photon emission  $t_h$  and at the end of the data set ( $t_{\max}$ ) to reflect the movement of the source.

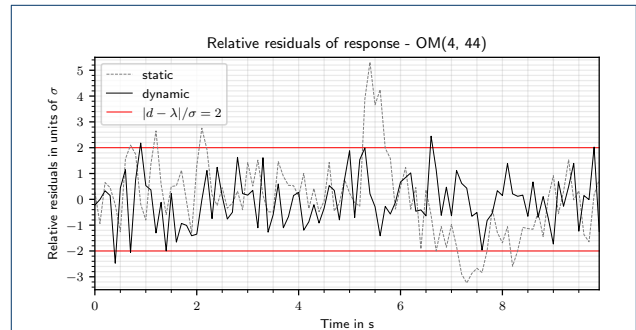
Observable	Ground truth	Run 1	Run 2	Run 3
$x(t_0)$ source position (m)	50.00	$49.89 \pm 0.08$	$49.88 \pm 0.09$	$49.89 \pm 0.08$
$x(t_h)$ source position (m)	50.00	$49.96 \pm 0.05$	$49.96 \pm 0.05$	$49.96 \pm 0.05$
$x(t_{\max})$ source position (m)	50.00	$50.02 \pm 0.08$	$50.03 \pm 0.09$	$50.03 \pm 0.08$
$y(t_0)$ source position (m)	1.00	$0.92 \pm 0.06$	$0.91 \pm 0.06$	$0.95 \pm 0.06$
$y(t_h)$ source position (m)	1.00	$1.00 \pm 0.07$	$1.00 \pm 0.07$	$1.00 \pm 0.06$
$y(t_{\max})$ source position (m)	1.00	$1.07 \pm 0.12$	$1.07 \pm 0.13$	$1.04 \pm 0.09$
$z(t_0)$ source position (m)	23.00	$23.04 \pm 0.08$	$23.02 \pm 0.06$	$23.02 \pm 0.07$
$z(t_h)$ source position (m)	23.00	$23.00 \pm 0.04$	$23.00 \pm 0.04$	$23.00 \pm 0.04$
$z(t_{\max})$ source position (m)	23.00	$22.96 \pm 0.10$	$22.99 \pm 0.08$	$22.98 \pm 0.09$
Flash duration (s)	5.14	5.14	5.14	5.14
$\mathcal{L}_{\max}$ ( $10^{10}$ Hz)	3.71	$3.51 \pm 0.02$	$3.51 \pm 0.02$	$3.51 \pm 0.02$
Total emission ( $10^{10}$ photons flash $^{-1}$ )	5.20	4.92	4.93	4.93

**Table 10**

Model parameters of a dynamic inference source. The model is used to reconstruct the photon count data generated from a simulated static source.

Observable	Model	Model parameters
$v_i$ velocity	Correlated signal with $i \in \{x, y, z\}$	$\mu_v = 0 \frac{\text{m}}{\text{s}}, \sigma_v = 0.1 \frac{\text{m}}{\text{s}},$ $\sigma_v = 0.1 \frac{\text{m}}{\text{s}}$
$x$ position	Uniform	$x = (15 \text{ m}, 75 \text{ m})$
$y$ position	Uniform	$y = (-20 \text{ m}, 40 \text{ m})$
$z$ position	Uniform	$z = (15 \text{ m}, 35 \text{ m})$
Flash shape	Correlated signal	See <a href="#">appendix</a>

ANTARES detector for tracking individual organisms. A reasonable estimate of the movement could be reconstructed for a simulated light source moving linearly with a velocity  $v = 0.2 \frac{\text{m}}{\text{s}}$ . Although the reconstructed locations in  $y$  dimension display deviations from the ground truth, the residuals are close to the shot noise of the measurement process. These results show that a linear movement with a velocity  $v = 0.2 \frac{\text{m}}{\text{s}}$  is in principle resolvable, but is not free of systematics. Besides the degeneracies, which are already discussed in section 4.1, the angular acceptance has great impact on the positioning of a light source. The optical modules of the ANTARES detector have a wide angular acceptance [40]. Therefore, changes of the source position in non-radial directions do not lead to significant changes in the photon count numbers, which reduces

**Figure 4**

Comparison of relative residuals of a static (dashed, gray) and dynamic (solid, black) inference source. The synthetic data were generated from a simulated dynamic source. The red line marks deviations as large as twice the shot noise  $\sigma$  of a Poisson process.

the possibility to recognise position changes. Multiple optical modules with smaller angular acceptance might increase the spatial resolution. The reconstructed flash characteristics differ only slightly between the reconstruction with a static and a dynamic model as shown in table 12. Therefore, with regards to the bioluminescence flash lightcurves, both models are sufficient to reconstruct a reasonable estimate for velocities below  $v = 0.2 \frac{\text{m}}{\text{s}}$ .

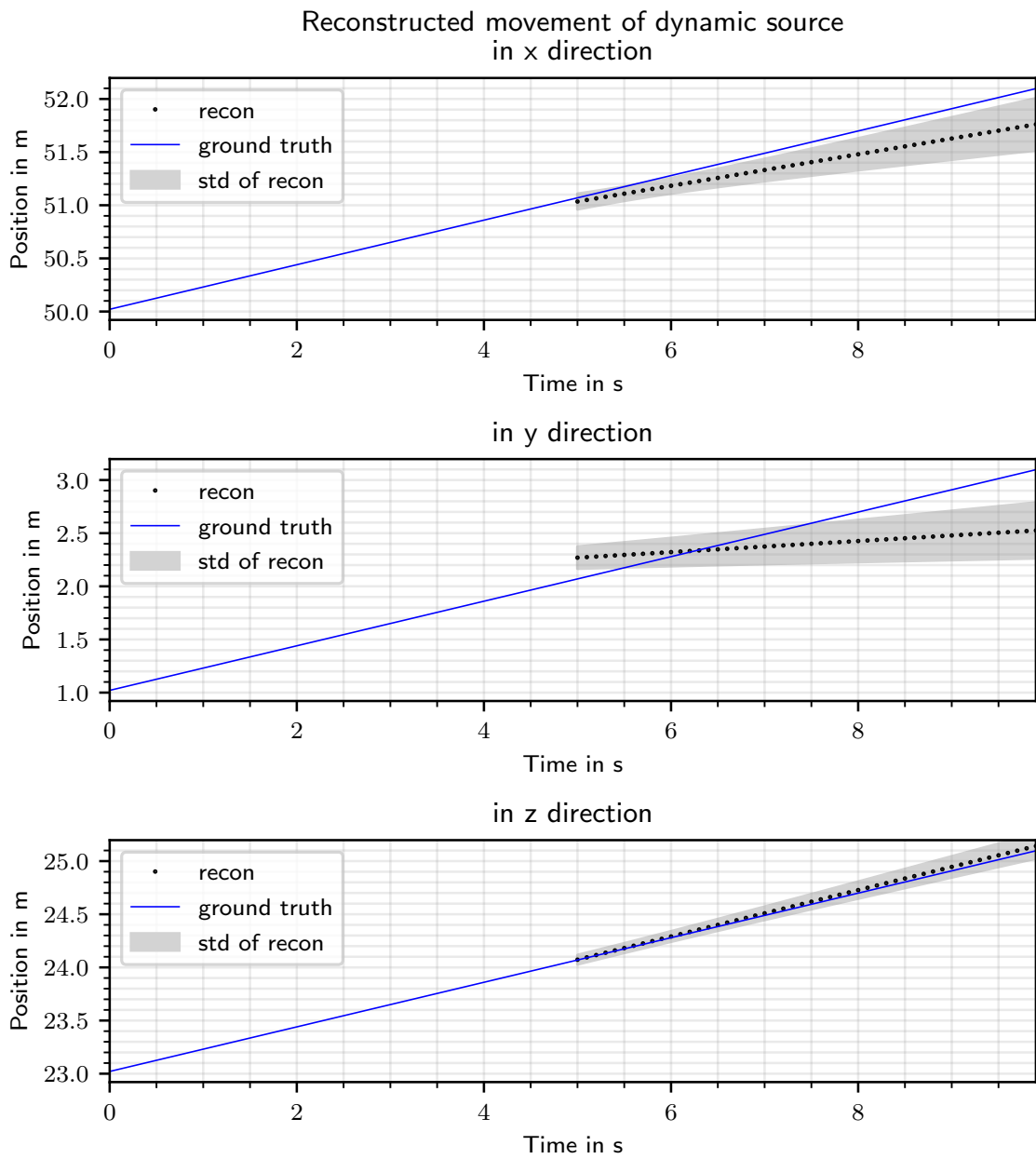


**Figure 5**

Reconstruction of the source position with the dynamic model. The simulated position (solid, blue) is shown in comparison to the reconstructed (circles, black) position. The reconstruction is only given for the time duration of the burst. Shown is also the uncertainty of the position reconstruction, shaded in gray.

**Table 11**

Ground truth and reconstructed parameters using a static source model. The synthetic photon count data were generated from a simulated dynamic source. The summary includes the reconstructed attenuation length.

Observable	Ground truth	Run 1	Run 2	Run 3
$x$ source position (m)	50.02 → 51.15 → 52.10	$51.64 \pm 0.04$	$50.80 \pm 0.03$	$51.14 \pm 0.05$
$y$ source position (m)	1.02 → 2.15 → 3.10	$1.79 \pm 0.06$	$2.65 \pm 0.04$	$2.25 \pm 0.05$
$z$ source position (m)	23.02 → 24.15 → 25.10	$23.98 \pm 0.03$	$24.55 \pm 0.03$	$24.30 \pm 0.02$
Flash duration (s)	5.14	5.14	5.14	5.14
$\mathcal{L}_{\max}$ ( $10^{10}$ Hz)	3.71	$3.49 \pm 0.02$	$3.28 \pm 0.02$	$3.99 \pm 0.03$
Total emission ( $10^{10}$ photons flash $^{-1}$ )	5.20	4.94	4.65	5.65
Attenuation length (m)	55.00	$59.98 \pm 0.06$	$59.92 \pm 0.24$	$45.12 \pm 0.45$

**Table 12**

Ground truth and reconstructed parameters using a dynamic source model. The synthetic photon count data were generated from a simulated dynamic source. The positions are given at the beginning of the observation period  $t_0$ , during the time of highest photon emission  $t_h$  and at the end of the data set ( $t_{\max}$ ) to reflect the movement of the source.

Observable	Ground truth	Run 1	Run 2	Run 3
$x(t_0)$ source position (m)	50.02	$50.29 \pm 0.30$	$50.02 \pm 0.13$	$49.89 \pm 0.12$
$x(t_h)$ source position (m)	51.15	$51.09 \pm 0.07$	$52.27 \pm 0.04$	$52.23 \pm 0.04$
$x(t_{\max})$ source position (m)	52.10	$51.76 \pm 0.24$	$54.15 \pm 0.10$	$54.17 \pm 0.10$
$y(t_0)$ source position (m)	1.02	$2.01 \pm 0.13$	$1.04 \pm 0.13$	$1.12 \pm 0.06$
$y(t_h)$ source position (m)	2.15	$2.29 \pm 0.11$	$3.31 \pm 0.05$	$3.33 \pm 0.05$
$y(t_{\max})$ source position (m)	3.10	$2.53 \pm 0.26$	$5.20 \pm 0.12$	$5.17 \pm 0.09$
$z(t_0)$ source position (m)	23.02	$22.98 \pm 0.12$	$22.92 \pm 0.08$	$22.92 \pm 0.12$
$z(t_h)$ source position (m)	24.15	$24.16 \pm 0.04$	$25.27 \pm 0.04$	$25.21 \pm 0.04$
$z(t_{\max})$ source position (m)	25.10	$25.14 \pm 0.12$	$27.22 \pm 0.10$	$27.30 \pm 0.12$
Flash duration (s)	5.14	5.14	5.14	5.14
$\mathcal{L}_{\max}$ ( $10^{10}$ Hz)	3.71	$3.55 \pm 0.02$	$3.61 \pm 0.03$	$3.59 \pm 0.03$
Total emission ( $10^{10}$ photons flash $^{-1}$ )	5.20	5.14	5.06	5.03

## 5 Data analysis

After presenting the possibilities and limitations of the method, the reconstruction routine is applied on data sets of the ANTARES Collaboration using different random seeds. The complete routine consists of a reconstruction using a static model and a dynamic model as explained in section 3.2.5. The outcomes of the static and dynamic reconstruction provide similar results regarding the position during the time of highest photon emission and the flash lightcurve. Therefore, it is sufficient to present only the results of the final step using the dynamic model.

For the reconstruction we rely on flash lightcurves that were detected over several storeys to be able to reduce the degeneracy. Since the process of finding such light emissions has not been automated, only a small excerpt of flash patterns found in the ANTARES data is analyzed here. We identified three suitable bioluminescence events in the data of early 2010, which we analyse in the following. The data samples cover observation times of 7 – 10 s. In table 13 we label the samples used for the following reconstructions and state the array of optical modules that detected the flash neglecting malfunctioning modules.

### 5.1 ANTARES recordings of flash 1

Starting with the 11th of January 2010 at 04:12:35 (UTC) a flash pattern was recorded by 16 optical mod-

**Table 13**

Data samples recorded by the ANTARES telescope reconstructed within this work.

Label	Time stamp (UTC)	OMs	Duration
Flash 1	11.1.2010, 04:12:35	(4, 34 – 51)	~ 10 s
Flash 2	11.1.2010, 04:13:20	(4, 37 – 54)	~ 9 s
Flash 3	19.1.2010, 22:28:10	(4, 34 – 51)	~ 7 s

ules over 5 storeys. The complete recording has already been shown in figure 2 in section 2. Flash 1 peaked at around 40 s after the start of the recording. Two optical modules, (4, 41) and (4, 51), within the optical module array (4, 37 – 51) did not record any photon counts. The model parameters used for the reconstruction are presented in table 14.

The reconstruction of the position and movement, as well as the characteristics of the bioluminescence lightcurve for four different random seeds, are summarized in table 16. For the reconstruction runs 2 – 4 we observe similar results. The results of the remaining run 1 deviate largely from the other ones, especially the  $y$  and  $z$  source positions differ more than 5 m. Even though, the reconstructed observables of run 1 are biologically plausible, the residuals of run 1 are larger compared to the runs 2 – 4. Therefore, we conclude that the runs 2 – 4 yield better estimates.

The uncertainty estimates are significantly smaller than the deviations between the reconstruction runs.

**Table 14**

Model parameters for the dynamic source model, the ANTARES telescope and its surroundings on the 11th of January 2010 at 04:12 (UTC). This model is used to reconstruct biological sources detected by the ANTARES telescope on 11th of January 2010 at 04:12 (UTC) and 04:13 (UTC), that emitted flash 1 and 2.

Observable	Model	Model parameter
$\epsilon$	$\mathcal{G}(\epsilon - \mu_\epsilon, \sigma_\epsilon^2)$ with $\mathcal{G}(\sigma_\epsilon - \mu_{\sigma_\epsilon}, \sigma_{\sigma_\epsilon}^2)$	$\mu_\epsilon = \epsilon_{\text{ANTARES}}$ $\mu_{\sigma_\epsilon} = 0.05,$ $\sigma_{\sigma_\epsilon} = 0.01$
$l_{\text{att}}$	$\mathcal{U}(l_{\text{min}}, l_{\text{max}})$	$l_{\text{min}} = 45 \text{ m},$ $l_{\text{max}} = 60 \text{ m}$
$n_{\text{storey}}$	$\mathcal{G}(n_{\text{storey}} - \mu_n, \sigma_n^2)$	$\mu_n = 50 \text{ kHz},$ $\sigma_n = 5 \text{ kHz}$
$x$ position	Uniform	$x = (15 \text{ m}, 75 \text{ m})$
$y$ position	Uniform	$y = (-20 \text{ m}, 30 \text{ m})$
$z$ position	Uniform	$z = (15 \text{ m}, 35 \text{ m})$
$v_i$ velocity	Correlated signal with $i \in \{x, y, z\}$	$\mu_v = 0, \sigma_v = 0.1,$ $\sigma_{\sigma_v} = 0.05$
Flash shape	Correlated signal	See <a href="#">appendix</a>

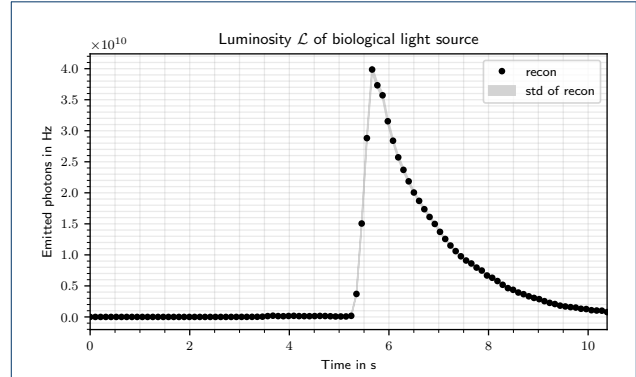
As mentioned in section 3, because of the mismatch between the assumed model and the real data generation, the MGVI algorithm can not calculate reasonable uncertainty estimates. The given uncertainties do not include systematic errors. Therefore, these estimates are not given for the following data analysis, since they are not representative.

In figure 6, the reconstructed flash lightcurve of run 2 is presented as it provides the smallest data residuals. We also illustrate the estimated movement in figure 7.

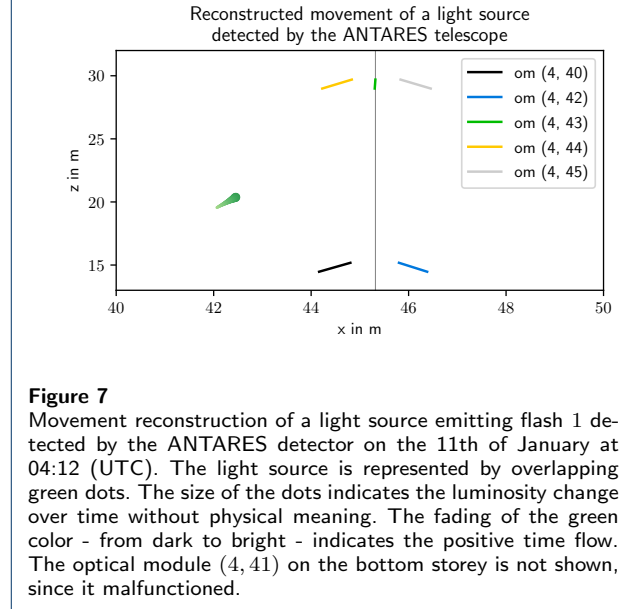
## 5.2 ANTARES recordings of flash 2

A second flash was observed on the same day at 04:13:20 (UTC) recorded by optical modules within the array (4, 37 – 54). Flash 2 peaked at around 85 s after the start of the recording shown in figure 2 in section 2. The optical modules (4, 41) and (4, 51) did not detect the second flash as they already did not record counts during the first flash. Furthermore, optical module (4, 43) did not record any photon for the period of highest luminosity, since the readout electronics were saturated. All model parameters are the same as for flash 1 given in table 14. The ANTARES detector is still in a similar configuration, because the second flash occurred around one minute later. Furthermore, due to similar photon count data of flash 1 and flash 2, the same a priori assumption of the position can be taken.

The results of the different runs are summarized in table 17. Two different types of reconstructions can be observed; run 2 and 4 reconstructed a rapid movement, whereas run 1 and 3 estimate smaller changes in the position. Since the rapid movement for run 2 and 4 occurs before the actual flash was emitted, no reasonable estimate can be made for this period. When comparing

**Figure 6**

Reconstruction of the bioluminescence flash 1 lightcurve detected by the ANTARES detector on the 11th of January 2010 at 04:12 (UTC).

**Figure 7**

Movement reconstruction of a light source emitting flash 1 detected by the ANTARES detector on the 11th of January at 04:12 (UTC). The light source is represented by overlapping green dots. The size of the dots indicates the luminosity change over time without physical meaning. The fading of the green color - from dark to bright - indicates the positive time flow. The optical module (4, 41) on the bottom storey is not shown, since it malfunctioned.

the reconstructed positions after the luminosity peak, we observe similar movements.

In figure 8 we present the flash lightcurve of run 1, since the smallest data residuals could be calculated for this run. The reconstructed movement of run 1 is illustrated in figure 9.

The second flash occurred only 44 seconds after and around 13 m away from the first flash. A causal connection between both light emission is likely. Due to the temporal and spatial closeness of the two events, it can not be excluded that the light was emitted by the same organism. But the deviation between the lightcurve structures of the two flashes also allow the assumption of a recorded communication of two organisms.

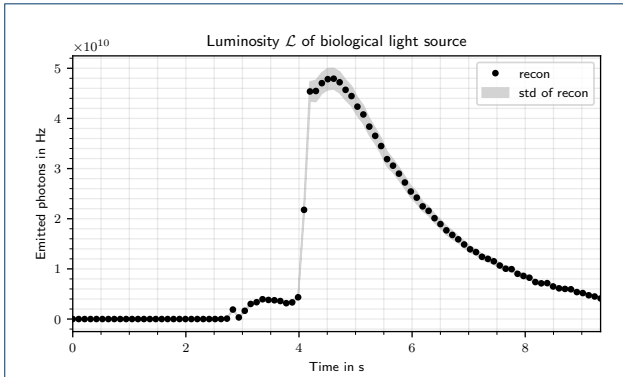


**Figure 8** Reconstruction of the emitted bioluminescence flash 2 lightcurve detected by the ANTARES detector on the 11th of January 2010 at 04:13 (UTC).

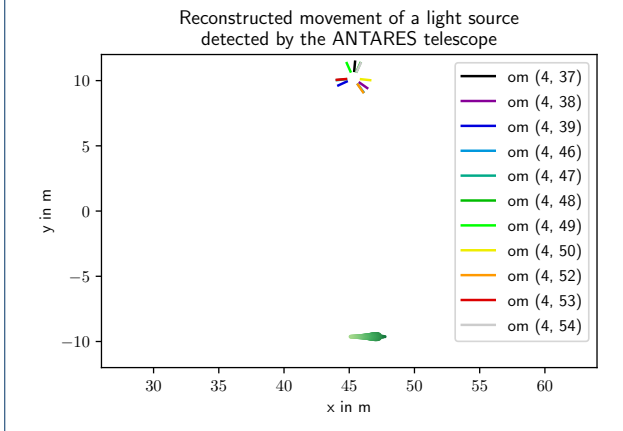


**Figure 9** Movement reconstruction of a light source emitting flash 2 detected by the ANTARES detector on the 11th January at 04:13. The light source is represented by overlapping green dots. The size of the dots indicates the luminosity change over time without physical meaning. The fading of the green color - from dark to bright - indicates the positive time flow.

### 5.3 ANTARES recordings of flash 3

The last bioluminescence flash that is analyzed within this work occurred on the 19th of January 2010 at 22:28 (UTC). In comparison to the previous models we adjust the position model parameter since the flash was detected by different optical modules. The position model parameters are given in table 15. The remaining model parameters are the same as in table 14.

Table 18 summarizes the reconstruction runs and clearly shows that run 1 deviates from the other reconstructions. By calculating the estimated velocity of the source as  $3.8 \frac{m}{s}$  the result can be classified as biologically implausible [48]. Besides that, the data residuals are higher compared to the runs 2 – 4, we hence can conclude that this run resulted in a worse fit to the data. Therefore, as a reasonable reconstruction result

**Table 15**

Model parameters for the initial position of a dynamic source. The model is used to reconstruct a biological source detected by the ANTARES telescope on the 19th of January 2010 at 22:28 (UTC) that emitted flash 3. The other model parameters are taken from table 14.

Observable	Model	Model parameter
$x$ position	Uniform	$x = (-25 \text{ m}, 35 \text{ m})$
$y$ position	Uniform	$y = (65 \text{ m}, 125 \text{ m})$
$z$ position	Uniform	$z = (-40 \text{ m}, 10 \text{ m})$

the flash lightcurve of run 2 is presented in figure 10 and the reconstructed movement of this run illustrated in figure 11.

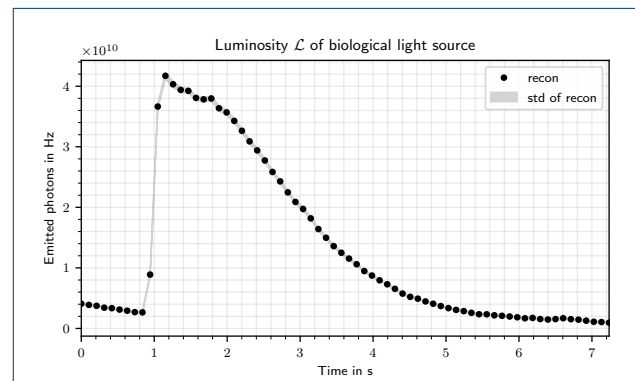


**Figure 10** Reconstruction of the emitted bioluminescence flash 3 lightcurve detected by the ANTARES detector on the 19th of January 2010 at 22:28 (UTC).

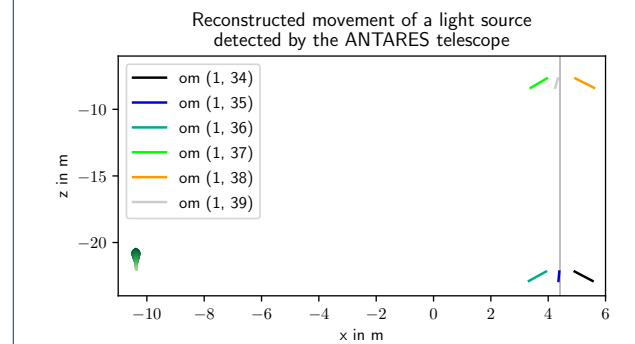


**Figure 11** Movement reconstruction of a light source emitting flash 3 detected by the ANTARES detector on the 19th of January at 22:28 (UTC). The light source is colored green. The size of the dots indicates the luminosity change over time without physical meaning. The fading of the green color - from dark to bright - indicates the positive time flow.

## 6 Discussion

The application of the method on synthetic and real data reveals both the strengths and the limitations of our approach. The reconstruction of the flash

**Table 16**

Reconstructed parameters assuming a dynamic light source model. The flash 1 lightcurve used for the reconstruction was recorded on the 11th of January 2010 at 04:12 (UTC) by the ANTARES telescope. The positions are given at different times as in table 12.

Observable	Run 1	Run 2	Run 3	Run 4
$x(t_0)$ source position (m)	45.35 ± 0.00	42.92 ± 0.25	42.21 ± 0.23	43.79 ± 0.13
$x(t_h)$ source position (m)	45.35 ± 0.00	42.45 ± 0.12	42.53 ± 0.07	42.6 ± 0.09
$x(t_{\max})$ source position (m)	45.35 ± 0.00	42.06 ± 0.37	41.71 ± 0.14	41.62 ± 0.20
$y(t_0)$ source position (m)	10.88 ± 0.06	1.99 ± 0.07	2.19 ± 0.15	2.46 ± 0.15
$y(t_h)$ source position (m)	10.85 ± 0.06	2.00 ± 0.05	1.98 ± 0.09	2.05 ± 0.06
$y(t_{\max})$ source position (m)	10.82 ± 0.07	2.01 ± 0.08	1.81 ± 0.18	1.71 ± 0.15
$z(t_0)$ source position (m)	15.00 ± 0.00	21.37 ± 0.05	21.25 ± 0.24	21.04 ± 0.22
$z(t_h)$ source position (m)	15.19 ± 0.01	20.37 ± 0.05	20.41 ± 0.07	20.42 ± 0.07
$z(t_{\max})$ source position (m)	15.14 ± 0.01	19.54 ± 0.11	20.07 ± 0.12	19.9 ± 0.14
Flash duration (s)	5.14	5.14	5.14	5.14
$\mathcal{L}_{\max}$ ( $10^{10}$ Hz)	4.2 ± 0.02	3.99 ± 0.05	3.97 ± 0.04	3.93 ± 0.03
Total emission ( $10^{10}$ photons flash $^{-1}$ )	6.48	5.66	5.68	5.62

**Table 17**

Reconstructed parameters assuming a dynamic light source. The flash 2 lightcurve used for the reconstruction was recorded on the 11th of January 2010 at 04:13 (UTC) by the ANTARES telescope. The positions are given at different times as in table 12.

Observable	Run 1	Run 2	Run 3	Run 4
$x(t_0)$ source position (m)	48.90	49.27	48.81	49.78
$x(t_h)$ source position (m)	47.02	47.21	47.01	47.42
$x(t_{\max})$ source position (m)	45.10	45.01	45.17	44.90
$y(t_0)$ source position (m)	-9.63	-19.71	-9.61	-19.80
$y(t_h)$ source position (m)	-9.63	-10.62	-9.61	-13.15
$y(t_{\max})$ source position (m)	-9.63	-8.96	-9.61	-6.03
$z(t_0)$ source position (m)	19.46	19.26	19.56	15.15
$z(t_h)$ source position (m)	19.55	19.59	19.59	19.04
$z(t_{\max})$ source position (m)	19.65	19.93	19.62	20.06
Flash duration (s)	6.61	6.61	6.61	6.61
$\mathcal{L}_{\max}$ ( $10^{10}$ Hz)	4.79	5.51	4.81	6.69
Total emission ( $10^{10}$ photons flash $^{-1}$ )	11.83	13.09	11.87	14.27

**Table 18**

Reconstructed parameters assuming a dynamic light source model. The flash 3 lightcurve used for the reconstruction was recorded on the 19th of January 2010 at 22:28 (UTC) by the ANTARES telescope. The positions are given at different times as in table 12.

Observable	Run 1	Run 2	Run 3	Run 4
$x(t_0)$ source position (m)	-24.58	-10.38	-11.09	-10.39
$x(t_h)$ source position (m)	-20.59	-10.38	-11.11	-10.38
$x(t_{\max})$ source position (m)	0.48	-10.39	-11.21	-10.37
$y(t_0)$ source position (m)	110.44	104.40	104.81	104.39
$y(t_h)$ source position (m)	109.04	-104.42	104.85	104.43
$y(t_{\max})$ source position (m)	101.64	104.51	105.06	104.63
$z(t_0)$ source position (m)	-23.77	-20.60	-20.31	-20.54
$z(t_h)$ source position (m)	-23.06	-20.84	-20.54	-20.78
$z(t_{\max})$ source position (m)	-19.29	-22.10	-21.77	-22.03
Flash duration (s)	5.45	7.34	7.34	7.34
$\mathcal{L}_{\max}$ ( $10^{10}$ Hz)	12.26	4.17	5.32	4.18
Total emission ( $10^{10}$ photons flash $^{-1}$ )	18.55	9.41	12.31	9.49



lightcurve is limited by the remaining degeneracy between the efficiencies and attenuation length with the emitted photon numbers. Therefore, increasing the accuracy of the measurements of these quantities will allow more precise reconstructions of the total number of emitted photons.

Furthermore, the accuracy of the position reconstructions and the spatial resolution can be increased by reducing the angular acceptance and increasing the number of OMs. An OM with sharp angular acceptance is able to resolve small position changes more precisely, since changes of the angle between OMs and light source lead to significant changes in the arriving photon numbers. However, a small angular acceptance leads also to a smaller monitored volume, which can be compensated by using more OMs.

Although only a small number of photon data recorded by the ANTARES telescope has been analyzed in this study, the results already provide some insights on the biological sources. Our localizations of bioluminescence events showed that the light emitting organisms were sufficiently far from optical modules, so that they can be assumed to be undisturbed by them. Further measurements of the environment, e.g. sea current measurements, need to be taken into account to verify the occurrence of non-stimulated bioluminescence events. According to previous studies non-stimulated light emissions are rare [4, 7, 8, 33] and hardly distinguishable from stimulated ones using moving detectors [7]. Therefore, our method opens the possibility to study spontaneous and in-situ bioluminescence. Further analysis of data recorded by deep sea neutrino telescopes could give insights about the frequency and distribution of such spontaneous events and the occurrence of consecutive light emissions as already observed in this work.

## 7 Conclusion

This work shows the potential of bioluminescence studies with a neutrino telescope in the deep sea and highlights the biological activity information that can be extracted. But it also clearly points out the limitations of the bioluminescence studies in regards to the spatial resolution due to the architecture of the detector.

The proposed method is generic and can be applied on data sets of different underwater neutrino telescopes. The development and work on the new neutrino telescope in the Mediterranean Sea, KM3NeT [49], offers a detector architecture which is even more suitable for the study of luminescent organisms. Each optical module of KM3NeT will be equipped with 31 photomultiplier tubes having a narrower angular acceptance compared to the ANTARES setup [49]. This increases the spatial resolution of the positioning.

For future systematic surveys of bioluminescence the method needs to be automatized and optimized. An optimized framework can be used to build a catalogue of various types of bioluminescence lightcurves including the position of the source. In this work, we also showed that the tracking of light sources is possible. Therefore, this method can also be used to analyze the movement behavior of deep sea organisms, which still little is known about.

## Appendix

### Distribution transformation

Since the MGVI algorithm relies on standardized variables and therefore, the generative model is built on these variables, it is crucial to transform a Gaussian distribution with zero mean and unit covariance to specific distributions which are more reasonable for the mathematical model. Within this work the common transformations are between standardized Gaussian distributions and Gaussian distributions with given mean and covariance and between standardized Gaussian distributions and uniform distributions. The standardized variables are introduced as

$$\vec{\xi} \leftrightarrow \mathcal{G}(\vec{\xi}, \mathbb{I}). \quad (16)$$

The transformation  $s(\xi)$  from  $\vec{\xi}$  to  $\vec{s}$  sampled from a Gaussian distribution with given mean  $\vec{\mu}$  and correlation matrix  $C$  is given as

$$\vec{s} = s(\xi) = \vec{\mu} + \sqrt{C} \cdot \vec{\xi}. \quad (17)$$

Reducing the dimension to scalar values and also introducing a Gaussian distributed standard deviation  $\sigma \leftrightarrow \mathcal{G}(\sigma - \bar{\sigma}, \sigma_\sigma^2)$  gives the new transformation with Gaussian sampled standard deviation

$$s(\xi_\sigma, \xi) = \mu + \sigma \cdot \xi \quad (18)$$

$$= \mu + \underbrace{(\bar{\sigma} + \sigma_\sigma \cdot \xi_\sigma)}_{\sigma \leftrightarrow \mathcal{G}(\sigma - \bar{\sigma}, \sigma_\sigma^2)} \cdot \xi \quad (19)$$

A transformation from standardized variables to uniformly sampled variables  $s \leftrightarrow \mathcal{U}([t_0, t_1])$  can be done by using the cumulative distribution function (CDF) of a Gaussian distribution. Variables uniformly sampled from the range  $[0, 1]$  can be generated by the transformation

$$s([0, 1], \xi) = \text{CDF}(\xi). \quad (20)$$

By shifting and expanding, the standard uniform distribution can be transformed into any uniform distribution with range  $[t_0, t_1]$

$$s([t_0, t_1], \xi) = (t_1 - t_0) \cdot \text{CDF}(\xi) + t_0. \quad (21)$$

### Correlation matrix for luminosity bursts

According to the Wiener-Khinchin Theorem, a statistical homogeneous and isotropic signal  $s$  drawn from a Gaussian prior  $\mathcal{G}(s - \mu_s, S)$  with stationary auto-correlation  $S^{t_i t_j} = S^{ij} = C_s(t_i - t_j)$  becomes diagonal in Fourier space,

$$S^{ij} = (2\pi)^u \delta(w - w') C_s(w), \quad (22)$$

with  $\Delta = t_i - t_j$  and  $C_s(w) = \int d\Delta e^{i w \Delta} C_s(\Delta)$  as the Fourier transformed auto-correlation function.  $C_s(w)$  is identical to the power spectrum per time length  $T$ ,  $P_s(w) = \lim_{T \rightarrow \infty} \frac{1}{T} \left\langle \left| \int_T dt s^t e^{i w t} \right|^2 \right\rangle = C_s(w)$  [36].

Therefore, the covariance can be described efficiently by defining a power spectrum per time length  $T$ . In the following the power spectrum used to sample the luminosity bursts is discussed. Recall, that the signal  $s$  sampled with a given power spectrum is exponentiated to produce the bursts.

Instead of an inferable power spectrum, as used for the velocity vector, a fixed power spectrum has shown to be sufficient to reproduce the burst shapes and this assumption also reduces the computation time.

Power spectra of the form

$$P_s(w) = [A_s(w)]^2 = \frac{b}{\omega^p} \quad (23)$$

are used within this work with  $A_s(w)$  defined as amplitude. The amplitude is divided into two parts, the zero mode  $A_0$  and the remaining part  $A_s(w)$  with  $\omega > 0$ . Intuitive parameters  $a_0, b, p$  are introduced. Following relations ensure definitions of power spectra to be independent of the size of the total time length  $T$ . The zero mode  $A_0$  is defined by a relative zero mode  $a_0$  and given as

$$A_0 = \frac{a_0}{T}. \quad (24)$$

The remaining part of the amplitude is defined by the power law  $p$  and an amplitude factor  $b$ . The relation is given by

$$A_s(w) = \frac{b}{T \sqrt{\sum_{\omega' \neq 0} r(\omega')^2}} \cdot r(\omega) \quad (25)$$

with  $r(\omega) = \frac{1}{\omega^p}$  and  $\omega > 0$ . The parameters  $a_0, b$  and  $p$  are set by the user.

The table 19 provides a summary of variables defining the luminosity burst shape. Their use is briefly explained and the values used within this work are given.

**Table 19**

Summary of parameters used for the correlated log-signal of luminosity bursts.

Parameter	Value	Explanation
Amplitude factor $b$	8.0	Changes the magnitude of the fluctuations
Power law $p$	1.5	Changes the smoothness of the burst
Relative zero mode $a_0$	2.0	Coupled to the variance of the mean $\mu_s$
Mean $\mu_s$	4.0	Mean of the signal

### Acknowledgements

SH acknowledges funding from the European Research Council (ERC) under the European Union's Horizon 2020 research and innovation programme (grant agreement No 772663)

The authors acknowledge the financial support of the funding agencies: Centre National de la Recherche Scientifique (CNRS), Commissariat à l'énergie atomique et aux énergies alternatives (CEA), Commission Européenne (FEDER fund and Marie Curie Program), Institut Universitaire de France (IUF), LabEx UnivEarthS (ANR-10-LABX-0023 and ANR-18-IDEX-0001), Région Île-de-France (DIM-ACAV), Région Alsace (contrat CPER), Région Provence-Alpes-Côte d'Azur, Département du Var and Ville de La Seyne-sur-Mer, France; Bundesministerium für Bildung und Forschung (BMBF), Germany; Istituto Nazionale di Fisica Nucleare (INFN), Italy; Nederlandse organisatie voor Wetenschappelijk Onderzoek (NWO), the Netherlands; Council of the President of the Russian Federation for young scientists and leading scientific schools supporting grants, Russia; Executive Unit for Financing Higher Education, Research, Development and Innovation (UEFISCDI), Romania; Ministerio de Ciencia, Innovación, Investigación y Universidades (MCIU): Programa Estatal de Generación de Conocimiento (refs. PGC2018-096663-B-C41, -A-C42, -B-C43, -B-C44) (MCIU/FEDER), Generalitat Valenciana: Prometeo (PROMETEO/2020/019), Grisolia (ref. GRISOLIA/2018/119) and GenT (refs. CIDEAGENT/2018/034, /2019/043, /2020/049) programs, Junta de Andalucía (ref. ref. A-FQM-053-UGR18), La Caixa Foundation (ref. LCF/BQ/IN17/11620019), EU: MSC program (ref. 101025085), Spain; Ministry of Higher Education, Scientific Research and Professional Training, Morocco. We also acknowledge the technical support of Ifremer, AIM and Foselev Marine for the sea operation and the CC-IN2P3 for the computing facilities.

### Author details

<sup>1</sup>Information Field Theory Group, Max Planck Institute for Astrophysics, Garching, Germany. <sup>2</sup>Informatics 6 Chair of Robotics, Artificial Intelligence and Real time Systems, Technical University of Munich, Garching, Germany. <sup>3</sup>Department of Astrophysics/IMAPP, Radboud University Nijmegen, Nijmegen, Netherlands. <sup>4</sup>Department of Physics, Ludwig-Maximilians University, Munich, Germany. <sup>5</sup>CERN, Geneva, Switzerland. <sup>6</sup>Université de Strasbourg, CNRS, IPHC UMR 7178, F-67000 Strasbourg, France. <sup>7</sup>Université de Haute Alsace, F-68200 Mulhouse, France. <sup>8</sup>IFIC - Instituto de Física Corpuscular (CSIC - Universitat de València) c/ Catedrático José Beltrán, 2 E-46980 Paterna, Valencia, Spain. <sup>9</sup>Technical University of Catalonia, Laboratory of Applied Bioacoustics, Rambla Exposició, 08800 Vilanova i la Geltrú, Barcelona, Spain. <sup>10</sup>INFN - Sezione di Genova, Via Dodecaneso 33, 16146 Genova, Italy. <sup>11</sup>Friedrich-Alexander-Universität Erlangen-Nürnberg, Erlangen Centre for Astroparticle Physics, Erwin-Rommel-Str. 1, 91058 Erlangen, Germany. <sup>12</sup>Institut d'Investigació per a la Gestió Integrada de les Zones Costaneres (IGIC) - Universitat Politècnica de València. C/ Paranímf 1, 46730 Gandia, Spain. <sup>13</sup>Aix Marseille Univ, CNRS/IN2P3, CPPM, Marseille, France. <sup>14</sup>Université de Paris, CNRS, Astroparticule et Cosmologie, F-75013 Paris, France. <sup>15</sup>Aix Marseille Univ, CNRS, CNES, LAM, Marseille, France. <sup>16</sup>National Center for Energy Sciences and Nuclear Techniques, B.P.1382, R. P.10001 Rabat, Morocco. <sup>17</sup>University Mohammed V in Rabat, Faculty of Sciences, 4 av. Ibn Battouta, B.P. 1014, R.P. 10000 Rabat, Morocco. <sup>18</sup>INFN - Laboratori Nazionali del Sud (LNS), Via S. Sofia 62, 95123 Catania, Italy. <sup>19</sup>University Mohammed I, Laboratory of Physics of Matter and Radiations, B.P.717, Oujda 6000, Morocco. <sup>20</sup>Nikhef, Science Park, Amsterdam, The Netherlands. <sup>21</sup>Institute of Space Science, RO-077125

- Bucharest, Măgurele, Romania. <sup>22</sup>Universiteit van Amsterdam, Instituut voor Hoge-Energie Fysica, Science Park 105, 1098 XG Amsterdam, The Netherlands. <sup>23</sup>INFN - Sezione di Roma, P.le Aldo Moro 2, 00185 Roma, Italy. <sup>24</sup>Dipartimento di Fisica dell'Università La Sapienza, P.le Aldo Moro 2, 00185 Roma, Italy. <sup>25</sup>LPHEA, Faculty of Science - Semlali, Cadi Ayyad University, P.O.B. 2390, Marrakech, Morocco. <sup>26</sup>INFN - Sezione di Bologna, Viale Bertini-Pichat 6/2, 40127 Bologna, Italy. <sup>27</sup>INFN - Sezione di Bari, Via E. Orabona 4, 70126 Bari, Italy. <sup>28</sup>Department of Computer Architecture and Technology/CITIC, University of Granada, 18071 Granada, Spain. <sup>29</sup>Géozur, UCA, CNRS, IRD, Observatoire de la Côte d'Azur, Sophia Antipolis, France. <sup>30</sup>Dipartimento di Fisica dell'Università, Via Dodecaneso 33, 16146 Genova, Italy. <sup>31</sup>Université Paris-Sud, 91405 Orsay Cedex, France. <sup>32</sup>Dipartimento di Fisica e Astronomia dell'Università, Viale Bertini Pichat 6/2, 40127 Bologna, Italy. <sup>33</sup>Laboratoire de Physique Corpusculaire, Clermont Université, Université Blaise Pascal, CNRS/IN2P3, BP 10448, F-63000 Clermont-Ferrand, France. <sup>34</sup>LIS, UMR Université de Toulon, Aix Marseille Université, CNRS, 83041 Toulon, France. <sup>35</sup>Royal Netherlands Institute for Sea Research (NIOZ), Landsdiep 4, 1797 SZ 't Horntje (Texel), the Netherlands. <sup>36</sup>International Centre for Radio Astronomy Research - Curtin University, Bentley, WA 6102, Australia. <sup>37</sup>Huygens-Kamerlingh Onnes Laboratorium, Universiteit Leiden, The Netherlands. <sup>38</sup>Institut für Theoretische Physik und Astrophysik, Universität Würzburg, Emil-Fischer Str. 31, 97074 Würzburg, Germany. <sup>39</sup>Dr. Remeis-Sternwarte and ECAP, Friedrich-Alexander-Universität Erlangen-Nürnberg, Sternwartstr. 7, 96049 Bamberg, Germany. <sup>40</sup>Mediterranean Institute of Oceanography (MIO), Aix-Marseille University, 13288, Marseille, Cedex 9, France; Université du Sud Toulon-Var, CNRS-INSU/IRD UM 110, 83957, La Garde Cedex, France. <sup>41</sup>INFN - Sezione di Catania, Via S. Sofia 64, 95123 Catania, Italy. <sup>42</sup>Dpto. de Física Teórica y del Cosmos & C.A.F.P.E., University of Granada, 18071 Granada, Spain. <sup>43</sup>IRFU, CEA, Université Paris-Saclay, F-91191 Gif-sur-Yvette, France. <sup>44</sup>INFN - Sezione di Napoli, Via Cintia 80126 Napoli, Italy. <sup>45</sup>Museo Storico della Fisica e Centro Studi e Ricerche Enrico Fermi, Piazzale del Viminale 1, 00184, Roma. <sup>46</sup>INFN - CNAF, Viale C. Bertini Pichat 6/2, 40127, Bologna. <sup>47</sup>Institut Universitaire de France, 75005 Paris, France. <sup>48</sup>Dipartimento di Fisica dell'Università Federico II di Napoli, Via Cintia 80126, Napoli, Italy.
- References**
- Martini, S., Haddock, S.: Quantification of bioluminescence from the surface to the deep sea demonstrates its predominance as an ecological trait. *Scientific Reports* **7**(45750) (2017). doi:[10.1038/srep45750](https://doi.org/10.1038/srep45750)
  - Widder, E.A.: Bioluminescence in the Ocean: Origins of Biological, Chemical, and Ecological Diversity. *Science* (New York, N.Y.) **328**(5979), 704–708 (2010). doi:[10.1126/science.1174269](https://doi.org/10.1126/science.1174269)
  - Herren, C.M., Haddock, S.H.D., Johnson, C., Orrico, C.M., Moline, M.A., Case, J.F.: A multi-platform bathyphotometer for fine-scale, coastal bioluminescence research. *Limnology and Oceanography: Methods* **3**(5), 247–262 (2005). doi:[10.4319/lom.2005.3.247](https://doi.org/10.4319/lom.2005.3.247)
  - Martini, S., Nerini, D., Tamburini, C.: Relation between deep bioluminescence and oceanographic variables: A statistical analysis using time-frequency decompositions. *Progress in Oceanography* **127**, 117–128 (2014). doi:[10.1016/j.pocean.2014.07.003](https://doi.org/10.1016/j.pocean.2014.07.003)
  - Martini, S., Kuhn, L., Mallefet, J., Haddock, S.: Distribution and quantification of bioluminescence as an ecological trait in the deep sea benthos. *Scientific Reports* **9**(14654) (2019). doi:[10.1038/s41598-019-50961-z](https://doi.org/10.1038/s41598-019-50961-z)
  - Frank, T., Johnsen, S., Cronin, T.: Light and vision in the deep-sea benthos: II. Vision in deep-sea crustaceans. *The Journal of experimental biology* **215**, 3344–53 (2012). doi:[10.1242/jeb.072033](https://doi.org/10.1242/jeb.072033)
  - Priede, I., Bagley, P., Way, S., Herring, P.J., Partridge, J.: Bioluminescence in the deep sea: Free-fall lander observations in the Atlantic Ocean off Cape Verde. *Deep Sea Research Part I: Oceanographic Research Papers* **53**(7), 1272–1283 (2006). doi:[10.1016/j.dsr.2006.05.004](https://doi.org/10.1016/j.dsr.2006.05.004)
  - Widder, E.A., Bernstein, S.A., Bracher, D.F., Case, J.F., Reisenbichler, K.R., J. J. Torres, J.J., Robison, B.H.: Bioluminescence in the Monterey Submarine Canyon: image analysis of video recordings from a midwater submersible. *Marine Biology* **100**, 541–551 (1989). doi:[10.1007/BF00394831](https://doi.org/10.1007/BF00394831)
  - Craig, J., Priede, I., Aguzzi, J., Jamieson, A.: Abundant bioluminescent sources of low-light intensity in the deep Mediterranean Sea and North Atlantic Ocean. *Marine Biology* **162**(8) (2015). doi:[10.1007/s00227-015-2700-2](https://doi.org/10.1007/s00227-015-2700-2)
  - Messié, M., Shulman, I., Martini, S., Haddock, S.H.D.: Using fluorescence and bioluminescence sensors to characterize auto- and heterotrophic plankton communities. *Progress in Oceanography* **171**, 76–92 (2019). doi:[10.1016/j.pocean.2018.12.010](https://doi.org/10.1016/j.pocean.2018.12.010)
  - Esaias, W.E., Curl Jr., H.C., Seliger, H.H.: Action spectrum for a low intensity, rapid photoinhibition of mechanically stimuable bioluminescence in the marine dinoflagellates *Gonyaulax catenella*, *G. acatenella*, and *G. tamarensis*. *Journal of Cellular Physiology* **82**(3), 363–372 (1973). doi:[10.1002/jcp.1040820306](https://doi.org/10.1002/jcp.1040820306)
  - Morin, J.G.: Coastal Bioluminescence: Patterns and Functions. *Bulletin of Marine Science* **33**(4), 787–817 (1983)
  - Galt, C.P., Sykes, P.F.: Sites of bioluminescence in the appendicularians *Oikopleuradioica* and *O. labradoriensis* (Urochordata: Larvacea). *Marine Biology* **77**, 155–159 (1983). doi:[10.1007/BF00396313](https://doi.org/10.1007/BF00396313)
  - Lapota, D., Losee, J.R.: Observations of bioluminescence in marine plankton from the Sea of Cortez. *Journal of Experimental Marine Biology and Ecology* **77**(3), 209–239 (1984). doi:[10.1016/0022-0981\(84\)90121-7](https://doi.org/10.1016/0022-0981(84)90121-7)
  - Galt, C., Grober, M., Sykes, P.: Taxonomic Correlates of Bioluminescence among Appendicularians (Urochordata: Larvacea). *Biological Bulletin* **168**, 125–134 (1985). doi:[10.2307/1541178](https://doi.org/10.2307/1541178)
  - Galt, C.P., Grober, M.S.: Total stimuable luminescence of Oikopleura houses (Urochordata, Larvacea). *Bulletin of Marine Science* **765**(2) (1985)
  - Herring, P.J.: Copepod luminescence. *Hydrobiologia* **167**, 183–195 (1988). doi:[10.1007/BF00026304](https://doi.org/10.1007/BF00026304)
  - Lapota, D., Geiger, M., Stiffey, A., Rosenberger, D., Young, D.: Correlation of planktonic bioluminescence with other oceanographic parameters from a Norwegian fjord. *Marine Ecology-progress Series* **55**, 217–227 (1989). doi:[10.3354/meps055217](https://doi.org/10.3354/meps055217)
  - Batchelder, H.P., Swift, E.: Estimated near-surface mesoplanktonic bioluminescence in the western North Atlantic during July 1986. *Limnology and Oceanography* **34**(1), 113–128 (1989). doi:[10.4319/lo.1989.34.1.0113](https://doi.org/10.4319/lo.1989.34.1.0113)
  - Buskey, E., Swift, E.: An encounter model to predict natural planktonic bioluminescence. *Limnology and Oceanography* **35**(7), 1469–1485 (1990). doi:[10.4319/lo.1990.35.7.1469](https://doi.org/10.4319/lo.1990.35.7.1469)
  - Batchelder, H., Swift, E., Van Keuren, J.R.: Diel patterns of planktonic bioluminescence in the northern Sargasso Sea. *Marine Biology* **113**, 329–339 (1992). doi:[10.1007/BF00347288](https://doi.org/10.1007/BF00347288)
  - Buskey, E.J.: Epipelagic planktonic bioluminescence in the marginal ice zone of the Greenland Sea. *Marine Biology* **113**, 689–698 (1992). doi:[10.1007/BF00349712](https://doi.org/10.1007/BF00349712)
  - Herring, P.J., Latz, M., Bannister, N.J., Widder, E.A.: Bioluminescence of the poecilostomatoid copepod *Oncaea confiera*. *Marine Ecology-progress Series* **94**, 297–309 (1993). doi:[10.3354/meps094297](https://doi.org/10.3354/meps094297)
  - Swift, E., Sullivan, J.M., Batchelder, H.P., Van Keuren, J., Vaillancourt, R.D., Bidigare, R.R.: Bioluminescent organisms and bioluminescence measurements in the North Atlantic Ocean near latitude 59.5°N, longitude 21°W. *Journal of Geophysical Research* **100**(C4), 6527–6548 (1995). doi:[10.1029/94JC01870](https://doi.org/10.1029/94JC01870)
  - Latz, M.I., Jeong, H.J.: Effect of red tide dinoflagellate diet on the bioluminescence of *Protoperdinium* spp. *Marine Ecology-progress Series* **132**, 275–285 (1996). doi:[10.3354/meps132275](https://doi.org/10.3354/meps132275)
  - Latz, M.I., Nauen, J.C., Rohr, J.: Bioluminescence response of four species of dinoflagellates to fully developed pipe flow. *Journal of Plankton Research* **26**(12), 1529–1546 (2004). doi:[10.1093/plankt/fbh141](https://doi.org/10.1093/plankt/fbh141)
  - Lapota, D.: Seasonal Changes of Bioluminescence in Photosynthetic and Heterotrophic Dinoflagellates at San Clemente Island, (2012). doi:[10.5772/35341](https://doi.org/10.5772/35341)
  - Valiadi, M., Iglesias-Rodriguez, M.D.: Understanding bioluminescence in dinoflagellates — how far have we come? *Microorganisms* **1**, 3–25 (2013). doi:[10.3390/microorganisms1010003](https://doi.org/10.3390/microorganisms1010003)
  - Johnsen, G., Candeloro, M., Berge, J., Moline, M.: Glowing in the dark: Discriminating patterns of bioluminescence from different taxa during the Arctic polar night. *Polar Biology* **37**(5) (2014). doi:[10.1007/s00300-014-1471-4](https://doi.org/10.1007/s00300-014-1471-4)

30. Cronin, H., Cohen, J., Berge, J., Johnsen, G., Moline, M.: Bioluminescence as an ecological factor during high Arctic polar night. *Scientific Reports* **6**(36374) (2016). doi:[10.1038/srep36374](https://doi.org/10.1038/srep36374)
31. Aguilar, J.A., Albert, A., Amram, P., Anghinolfi, M., Anton, G., Anvar, S., Ardellier-Desages, F.E., Aslanides, E., Aubert, J.-J., Azoulay, R., *et al.*: Transmission of light in deep sea water at the site of the Antares neutrino telescope. *Astroparticle Physics* **23**(1), 131–155 (2005). doi:[10.1016/j.astropartphys.2004.11.006](https://doi.org/10.1016/j.astropartphys.2004.11.006)
32. Aguzzi, J., Fanelli, E., Ciuffardi, T., *et al.*: Inertial bioluminescence rhythms at the Capo Passero (KM3NeT-Italia) site, Central Mediterranean Sea. *Scientific Reports* **7**(44938) (2017). doi:[10.1038/srep44938](https://doi.org/10.1038/srep44938)
33. Tamburini, C., Canals, M., Durrieu de Madron, X., Houpert, L., Lefeuvre, D., *et al.*: Deep-Sea Bioluminescence Blooms after Dense Water Formation at the Ocean Surface. *PLOS ONE* **8**(7), 1–10 (2013). doi:[10.1371/journal.pone.0067523](https://doi.org/10.1371/journal.pone.0067523)
34. van Haren, H., Taupier-Letage, I., Aguilar, J.A., Albert, A., Anghinolfi, M., Anton, G., Anvar, S., Ardid, M., Assis Jesus, A.C., Astraatmadja, T., *et al.*: Acoustic and optical variations during rapid downward motion episodes in the deep north-western Mediterranean Sea. *Deep Sea Research Part I: Oceanographic Research Papers* **58**(8), 875–884 (2011). doi:[10.1016/j.dsr.2011.06.006](https://doi.org/10.1016/j.dsr.2011.06.006)
35. Knollmüller, J., Enßlin, T.A.: Metric Gaussian Variational Inference (2020). [1901.11033](https://arxiv.org/abs/1901.11033)
36. Martin Reinecke, Theo Steininger, Marco Selig: NIFTy – Numerical Information Field Theory. <https://gitlab.mpcdf.mpg.de/ift/NIFTy>
37. Arras, P., Baltac, M., Enßlin, T.A., Frank, P., Hutschenreuter, S., Knollmüller, J., Leike, R., Newrzella, M.-N., Platz, L., Reinecke, M., *et al.*: Nifty5: Numerical information field theory v5. *Astrophysics Source Code Library* (2019)
38. Adrián-Martínez, S., Ageron, M., Aguilar, J.A., Samarai, I.A., Albert, A., André, M., Anghinolfi, M., Anton, G., Anvar, S., Ardid, M., *et al.*: The Positioning System of the ANTARES Neutrino Telescope. *Journal of Instrumentation* **7**(08), 08002–08002 (2012). doi:[10.1088/1748-0221/7/08/t08002](https://doi.org/10.1088/1748-0221/7/08/t08002)
39. Ageron, M., Aguilar, J.A., Al Samarai, I., Albert, A., Ameli, F., André, M., Anghinolfi, M., Anton, G., Anvar, S., Ardid, M., *et al.*: ANTARES: The first undersea neutrino telescope. *Nuclear Instruments and Methods in Physics Research Section A: Accelerators, Spectrometers, Detectors and Associated Equipment* **656**(1), 11–38 (2011). doi:[10.1016/j.nima.2011.06.103](https://doi.org/10.1016/j.nima.2011.06.103)
40. Amram, P., Anghinolfi, M., Anvar, S., Ardellier-Desages, F.E., Aslanides, E., Aubert, J.-J., Azoulay, R., Bailey, D., Basa, S., Battaglieri, M., *et al.*: The ANTARES optical module. *Nuclear Instruments and Methods in Physics Research Section A: Accelerators, Spectrometers, Detectors and Associated Equipment* **484**(1-3), 369–383 (2002). doi:[10.1016/S0168-9002\(01\)02026-5](https://doi.org/10.1016/S0168-9002(01)02026-5)
41. Aguilar, J.A., Albert, A., Ameli, F., Anghinolfi, M., Anton, G., Anvar, S., Aslanides, E., Aubert, J.-J., Barbarito, E., Basa, S., *et al.*: The data acquisition system for the ANTARES neutrino telescope. *Nuclear Instruments and Methods in Physics Research Section A: Accelerators, Spectrometers, Detectors and Associated Equipment* **570**(1), 107–116 (2007). doi:[10.1016/j.nima.2006.09.098](https://doi.org/10.1016/j.nima.2006.09.098)
42. Albert, A., André, M., Anghinolfi, M., Anton, G., Ardid, M., Aubert, J.-J., Aublin, J., Avgitas, T., Baret, B., Barrios-Martí, J., *et al.*: Long-term monitoring of the ANTARES optical module efficiencies using  $^{40}\text{K}$  decays in sea water. *The European Physical Journal C* **78**(8) (2018). doi:[10.1140/epjc/s10052-018-6132-2](https://doi.org/10.1140/epjc/s10052-018-6132-2)
43. Amram, P., Anghinolfi, M., Anvar, S., Ardellier-Desages, F.E., Aslanides, E., Aubert, J.-J., Azoulay, R., Bailey, D., Basa, S., Battaglieri, M., *et al.*: Sedimentation and fouling of optical surfaces at the ANTARES site. *Astroparticle Physics* **19**(2), 253–267 (2003). doi:[10.1016/S0927-6505\(02\)00202-5](https://doi.org/10.1016/S0927-6505(02)00202-5)
44. Amram, P., Anvar, S., Aslanides, E., Aubert, J.-J., Azoulay, R., Basa, S., Benhammou, Y., Bernard, F., Bertin, V., Billault, M., *et al.*: Background light in potential sites for the ANTARES undersea neutrino telescope. *Astroparticle Physics* **13**(2-3), 127–136 (2000). doi:[10.1016/S0927-6505\(99\)00118-8](https://doi.org/10.1016/S0927-6505(99)00118-8)
45. Adrián-Martínez, S., Al Samarai, I., Albert, A., André, M., Anghinolfi, M., Anton, G., Anvar, S., Ardid, M., Assis Jesus, A.C., Astraatmadja, T., *et al.*: Measurement of the group velocity of light in sea water at the ANTARES site. *Astroparticle Physics* **35**(9), 552–557 (2012). doi:[10.1016/j.astropartphys.2011.12.003](https://doi.org/10.1016/j.astropartphys.2011.12.003)
46. Knollmüller, J., Enßlin, T.A.: Encoding prior knowledge in the structure of the likelihood (2018). [1812.04403](https://arxiv.org/abs/1812.04403)
47. Arras, P., Frank, P., Haim, P., Knollmüller, J., Leike, R., Reinecke, M., Enßlin, T.: The variable shadow of M87\* (2020). [arXiv:2002.05218](https://arxiv.org/abs/2002.05218)
48. Priede, I.G.: *Deep-Sea Fishes: Biology, Diversity, Ecology and Fisheries*. Cambridge University Press, ??? (2017). doi:[10.1017/9781316018330](https://doi.org/10.1017/9781316018330)
49. Adrián-Martínez, S., Ageron, M., Aharonian, F., Aiello, S., Albert, A., Ameli, F., Anassontzis, E., Andre, M., Androulakis, G., Anghinolfi, M., *et al.*: Letter of intent for KM3NeT 2.0. *Journal of Physics G: Nuclear and Particle Physics* **43**(8), 084001 (2016). doi:[10.1088/0954-3899/43/8/084001](https://doi.org/10.1088/0954-3899/43/8/084001)